Materials Science & Engineering A 945 (2025) 149022

Contents lists available at ScienceDirect

Materials Science & Engineering A

journal homepage: www.elsevier.com/locate/msea

Precipitation and strengthening mechanisms in Cu-0.27wt.% Sc alloy: Linking thermomechanical treatment, microstructure and properties

Ramona Henle [a,*], Roham Talei [b], Sebastian M. Eich [b], Simon Kött [c], Julia Dölling [d], Gerrit Nandi [a], Andreas Zilly [e], Ulrich Prahl [f], Guido Schmitz [b]

[a] Faculty of Technology, Cooperative State University Heidenheim, Marienstraße 20, Heidenheim an der Brenz, 89518, Germany
[b] Institute of Materials Science, University of Stuttgart, Heisenberg-Straße 3, 70569, Stuttgart, Germany
[c] Institute for Materials and Material Technologies (IWWT), Pforzheim University, Tiefenbronner Straße 65, 75175, Pforzheim, Germany
[d] Institute of Vehicle Concepts, German Aerospace Center e.V. (DLR), Pfaffenwaldring 38–40, 70569, Stuttgart, Germany
[e] Faculty of Technology, Cooperative State University Stuttgart, Lerchenstraße 1, 70194, Stuttgart, Germany
[f] Institute of Metal Forming, Technische Universität Bergakademie Freiberg, Bernhard-von-Cotta Straße 4, 09599, Freiberg, Germany

ARTICLE INFO

Keywords:
Cu-Sc alloys
Atom probe tomography
Microstructure evolution
Strengthening mechanisms
Precipitation modeling

ABSTRACT

Enhanced mechanical and electrical conductivity of low alloyed Cu-Sc alloys were systematically investigated with a focus on precipitation, solid solution, and dislocation strengthening. A Cu-0.27 wt% Sc alloy subjected to 50 % cold rolling and peak aged for 0.5 h at 450 °C achieved a high yield strength of 434 MPa and a conductivity of 42.5 MS/m (73.3 % IACS). The microstructural evolution during aging was characterized by SEM, TEM, and APT, revealing the rapid formation of nanoscale, plate-like Cu_4Sc precipitates growing with increasing aging time. The enhanced precipitation response in cold-worked conditions was attributed to dislocation-assisted nucleation and solute flux driven by strain fields. A mechanistic strengthening model incorporating work, solid solution, and particle hardening accurately predicts the time-dependent mechanical response. The results underline the capability of Sc as an effective alloying element for high-strength, high-conductivity copper alloys. Based on the observed kinetics and mechanisms, a multi-stage thermomechanical treatment involving intermediate deformation steps is proposed to further exploit this strengthening potential.

1. Introduction

Copper alloys are essential in high-performance applications such as electrical systems, automotive components, and aerospace technologies, where a balance between mechanical strength and electrical conductivity is essential. While pure copper offers excellent electrical and thermal conductivity, its low strength limits structural applications [1]. Alloying increases strength but reduces conductivity due to electron scattering [2,3]. Solid solution hardening therefore presents a fundamental conflict between both properties [4]. In contrast, precipitation hardening strengthens copper alloys by forming nanoscale precipitates while reducing matrix solute content. During aging, conductivity generally rises, while strength peaks as particle strengthening competes with coarsening [5–7].

Precipitation-hardening alloys such as Cu-Cr [8], Cu-Zr [9] or Cu-Cr-Zr [10] achieve good strength-conductivity balance but are limited by low solubility and rapid precipitate coarsening, demanding precise process control. Rare earth elements have thus been explored as alternatives. For instance, Cu-Hf [11] and Cu-Cr-Hf [12] alloys form Cu_5Hf precipitates that improve strength with limited conductivity loss. However, Hf's still relatively high solubility in Cu at aging temperatures (0.04 wt% at 500 °C [2]) increases electron scattering by solutes. In comparison, scandium offers more favorable thermodynamics: high solubility at solution annealing temperatures (0.35 wt% at 865 °C [2, 13]) and very low solubility during aging (0.0065 wt% at 450 °C [14]), allowing rapid precipitation of fine precipitates. This promotes strengthening while preserving conductivity.

Hao et al. [15] investigated a Cu–0.4 wt% Sc alloy and mapped the precipitation sequence (solid solution → Sc-rich clusters → metastable Cu_4Sc → stable Cu_4Sc). Using cryogenic rolling and aging, they achieved 696 MPa yield strength and 62.8 % IACS conductivity, attributing the results to coherent and incoherent particle strengthening. Further studies by Franczak et al. [9], Dölling et al. [16,17] and Henle et al. [18] showed that cold deformation before aging accelerates precipitation and

* Corresponding author.
E-mail addresses: Ramona.Henle@dhbw-heidenheim.de, Ramona-Lucy.Henle@doktorand.tu-freiberg.de (R. Henle).

https://doi.org/10.1016/j.msea.2025.149022
Received 24 July 2025; Received in revised form 19 August 2025; Accepted 23 August 2025
Available online 25 August 2025

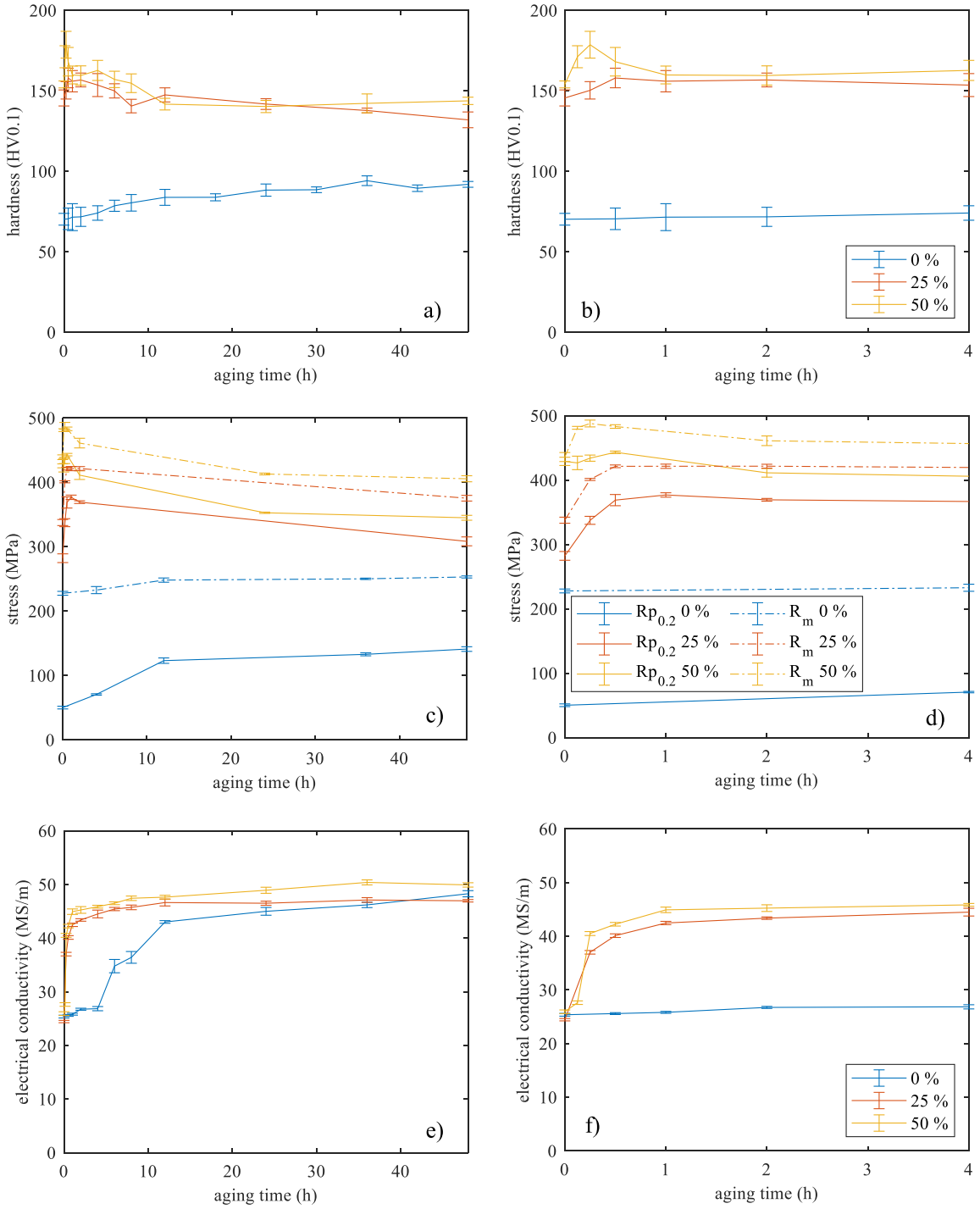

Fig. 1. Evolution of mechanical and electrical properties of the CuSc0.27 alloy during aging at 450 °C for up to 48 h from 0 %, 25 %, and 50 % cold-worked conditions: (a, b) Vickers hardness, (c, d) yield and tensile strength, (e, f) electrical conductivity; up to 48 h (a, c, e) and up to 4 h (b, d, f). Legends apply to the corresponding pair of plots in each row and are displayed in (b), (d), and (f).

lowers onset temperatures, enabling efficient processing. However, scandium's dual role as solute and precipitation agent remains unclear, especially in alloys with <0.3 wt% Sc. Prior studies often lacked resolution to distinguish solid solution, precipitation, and work hardening.

This study addresses the knowledge gap by systematically analyzing strengthening mechanisms in a Cu-0.27 wt% Sc alloy during aging. Atom probe tomography (APT) resolves precipitate evolution, while X-ray diffraction (XRD), electrical conductivity, hardness, and tensile testing provide quantitative input for mechanistic analysis. These insights advance understanding of strengthening interactions in Cu-Sc alloys and support the design of future high-performance materials.

2. Materials and methods

2.1. Specimen preparation

Binary Cu-Sc alloys with Sc concentrations up to 0.33 wt% were synthesized from Cu-OFE and a Cu-Sc9 master alloy by vacuum induction melting (VC400, Indutherm BluePower Casting Systems GmbH) at 1300 °C in a boron-nitride-coated graphite crucible and cast into a preheated graphite mold (400 °C, 10 mm thickness). To ensure homogeneity, the ingots underwent three cold-rolling passes (logarithmic strain $\varphi = 0.6$ each) with intermediate annealing at 870 °C for 10 min and 60 min (ME65/13, Helmut ROHDE GmbH). Final rolling to 1.5 mm was conducted in longitudinal direction using a duo mill (roll diameter 120 mm, 40 min^{-1}), followed by a final annealing at 870 °C for 60 min to ensure full recrystallization and maximize Sc solubility. Solution-treated specimens were water-quenched to room temperature.

Surface layers were removed post-treatment to prevent surface contamination. The chemical composition was verified by 18 measurements per specimen at three positions using a calibrated mobile optical emission spectrometer (SPECTROTEST, SPECTRO Analytical Instruments GmbH), confirming the Sc content within ±0.01 wt% of the target.

To investigate precipitation hardening, the solution-treated material was cold-rolled to 25 % and 50 % thickness reduction, followed by aging at 450 °C for up to 48 h. Accordingly, three conditions were evaluated: 0 %, 25 %, and 50 % cold-worked (CW).

2.2. Experimental methods

For microstructural characterization, specimens were sectioned using a precision cutting machine (Labotom 5, Struers) with water cooling, mounted in conductive resin, and prepared in longitudinal, transverse, and cross-sectional orientations. Grinding and polishing were performed on a Tegramin-30 system (Struers), followed by final vibratory polishing (Vibromet 2, Buehler) with 0.05 µm OP-S SiO_2 suspension for SEM and XRD analysis.

Microstructure was examined via field-emission scanning electron microscopy (FE-SEM, Gemini Sigma VP, Carl Zeiss Microscopy GmbH) equipped with a backscatter electron detector and energy-dispersive X-ray spectroscopy (EDS) (XFlash 6|30, Bruker Nano GmbH) at 10 kV. Grain size was evaluated using the linear intercept method (ASTM E112-13 [19]) on five equidistant cross-sections. Crystallographic texture was assessed via electron backscatter diffraction (GeminiSEM 450, Carl Zeiss Microscopy GmbH) using an AZtecHKL EBSD system (Oxford Instruments plc).

Electrical conductivity was measured by eddy current testing (Sigmascope SMP10, Helmut Fischer GmbH, with TF100A temperature compensation); ten repetitions per specimen ensured statistical confidence. Microhardness was measured with a Vickers hardness tester (NEXUS 412A, Innovatest GmbH) in accordance with DIN EN ISO 6507–1:2018–07 [20], Innovatest GmbH) using a test load of 0.980 N (HV0.1) and seven indentations per specimen.

Tensile properties were determined on a universal testing machine (Z100 TEW Allround-Line, ZwickRoell GmbH & Co. KG) equipped with a video extensometer (VideoXtens biax 2–150 HP, ZwickRoell) and a 100 kN load cell (Xforce K) under strain control (0.003 min^{-1}). Specimens were CNC milled (1 mm VHN Solid Carbide End Mill, rotation speed 1500 min^{-1}, speed rate 200 mm/min) parallel to the rolling direction under water to avoid thermal effects. The geometry followed Type H (non-proportional, DIN EN ISO 50125:2022-08 [21]), with a thickness of 0.75–1.5 mm (depending on prior cold deformation), width of 5 mm, and gauge length of 17 mm (see Appendix, Figure A1).

X-ray diffraction (XRD) was performed using an XRD 3000 TT diffractometer (Waygate Technologies) in Bragg–Brentano geometry with CoKα radiation (40 kV, 40 mA). Scans were conducted from 20° to 140° with 0.05° step size and 0.15°/min scan speed. Calibration used LaB_6. Peak fitting employed a pseudo-Voigt function (Rayflex–analyze 2.503, Waygate Technologies), and instrumental broadening was corrected using the integral breadth method. Micro-strain was determined by Williamson–Hall analysis.

Transmission electron microscopy (TEM) specimens were cut from 0.1 mm-thick lamellae (wire electro-discharge machining (EDM), high-purity Cu wire), ground, punched, and electropolished (Tenupol-5, Struers GmbH). Bright-field imaging was performed at 200 kV (CM-200 FEG, Philips).

For atom probe tomography (APT), additional needle-shaped specimens (0.1 mm × 0.1 mm) were prepared from the same sheets by EDM and electrochemically polished using Struers D2 electrolyte in three steps (7.5 V, 5 V, 2.5 V). Final apex diameters were below 100 nm.

APT was conducted on a custom-built system [22] under ultrahigh vacuum ($<10^{-9}$ mbar) at 80 K. Voltage pulses (100 kHz) and standing voltages up to 16 kV enabled field evaporation. A position-sensitive detector (50.5 % detection efficiency) captured time-of-flight and spatial coordinates, enabling 3D reconstructions with sub-nm resolution [23–25]. The mass spectra predominantly contained Cu and Sc, with minor H from residual chamber gas.

Data analysis and reconstruction was performed using The APyT Package [26]. Cluster identification and compositional analysis were performed using the OVITO software package [27]. The local atomic composition was calculated within a radius of 0.66 nm around each atom. Atoms exceeding 12.5 at.% were selected for further analysis to ensure a reliable detection of the Cu_4Sc phase. Clusters were identified by grouping neighboring atoms within 0.77 nm; only those containing $\geq$20 Sc atoms were retained for subsequent evaluation and visualization to reliably identify clusters representing the expected Cu_4Sc well within the resolution limit of APT.

3. Results

3.1. Mechanical and electrical properties

Fig. 1a shows the Vickers hardness evolution of CuSc0.27 aged at 450 °C for up to 48 h in three different cold-working conditions (0 %, 25 %, and 50 % thickness reduction by rolling). Initial hardness values reflect the solution-annealed and cold-rolled conditions prior to aging. Cold deformation significantly increased hardness from 70.2 HV0.1 to 145.6 HV0.1 (25 %) and 154.0 HV0.1 (50 %). Upon aging, cold-worked conditions exhibited rapid hardening, with peak values of 158.0 HV0.1 (25 % CW at 0.5 h) and 178.6 HV0.1 (50 % CW at 0.25 h), indicative of accelerated precipitation behavior. In the overaged state (48 h), hardness decreased moderately, while the 0 % CW condition showed a continuous increase up to 138.7 HV0.1, suggesting slower precipitation reaction in the absence of pre-deformation. Yield strength (YS) and ultimate tensile strength (UTS) follow trends similar to hardness (Fig. 1c). Cold work raised the initial YS to 282.2 MPa (25 %) and 423.1 MPa (50 %), compared to 51.3 MPa for the solution-annealed specimen. Aging led to a rapid strength increase, peaking at 443.1 MPa (YS) and 483.1 MPa (UTS) for 50 % CW after 0.5 h (Fig. 1d). The true UTS maximum (487.9 MPa) was observed at 0.25 h, concurrent with the hardness peak. The 25 % CW condition reached its maximum YS (376.8 MPa) and UTS (421.4 MPa) at 1 h. Strength in the 0 % CW sample increased gradually to 141.1 MPa (YS) and 253.1 MPa (UTS) after 48 h. These trends confirm that pre-deformation enhances precipitation and strengthening response. Stress–strain curves are shown in Appendix Fig. A2, relevant parameters derived from tensile tests are summarized in Appendix Tables A1 - A3. As shown in Fig. 1e–f, the initial electrical conductivity of all conditions was about 25.0 MS/m, limited by scattering from solute foreign atoms in the copper matrix. Cold deformation had no significant influence on the initial conductivity. During aging, conductivity increased as previous solute Sc atoms precipitated. The 50 % CW condition exhibited the fastest rise, reaching 50.4 MS/m after 36 h, with the 25 % CW state following a similar trend. Both cold-worked specimens

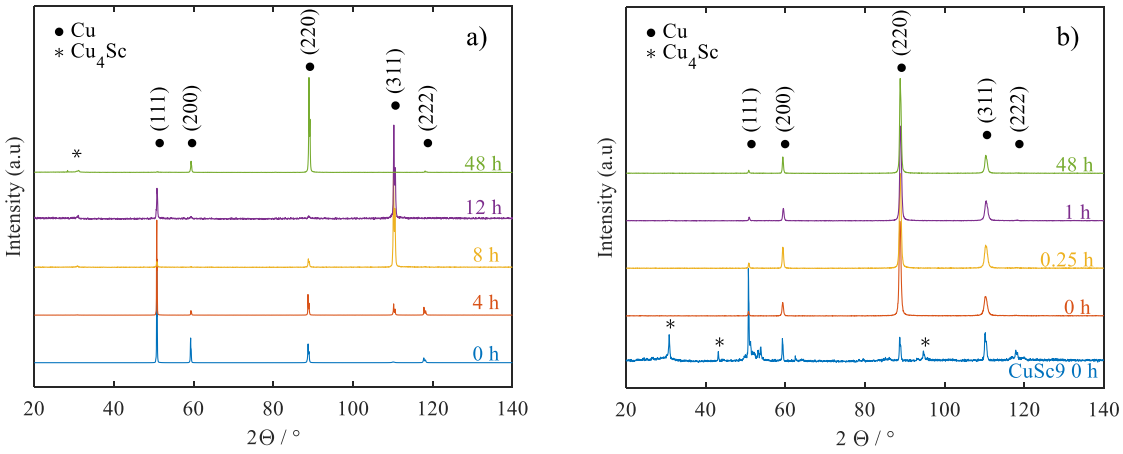

Fig. 2. XRD patterns of CuSc0.27 alloys aged at 450 °C: (a) 0 % cold-worked condition from solution-annealed to 48 h, (b) comparison of solution-annealed CuSc9 master alloy (0 % CW) and CuSc0.27 alloy after solution treatment and 50 % cold working, aged for indicated durations.

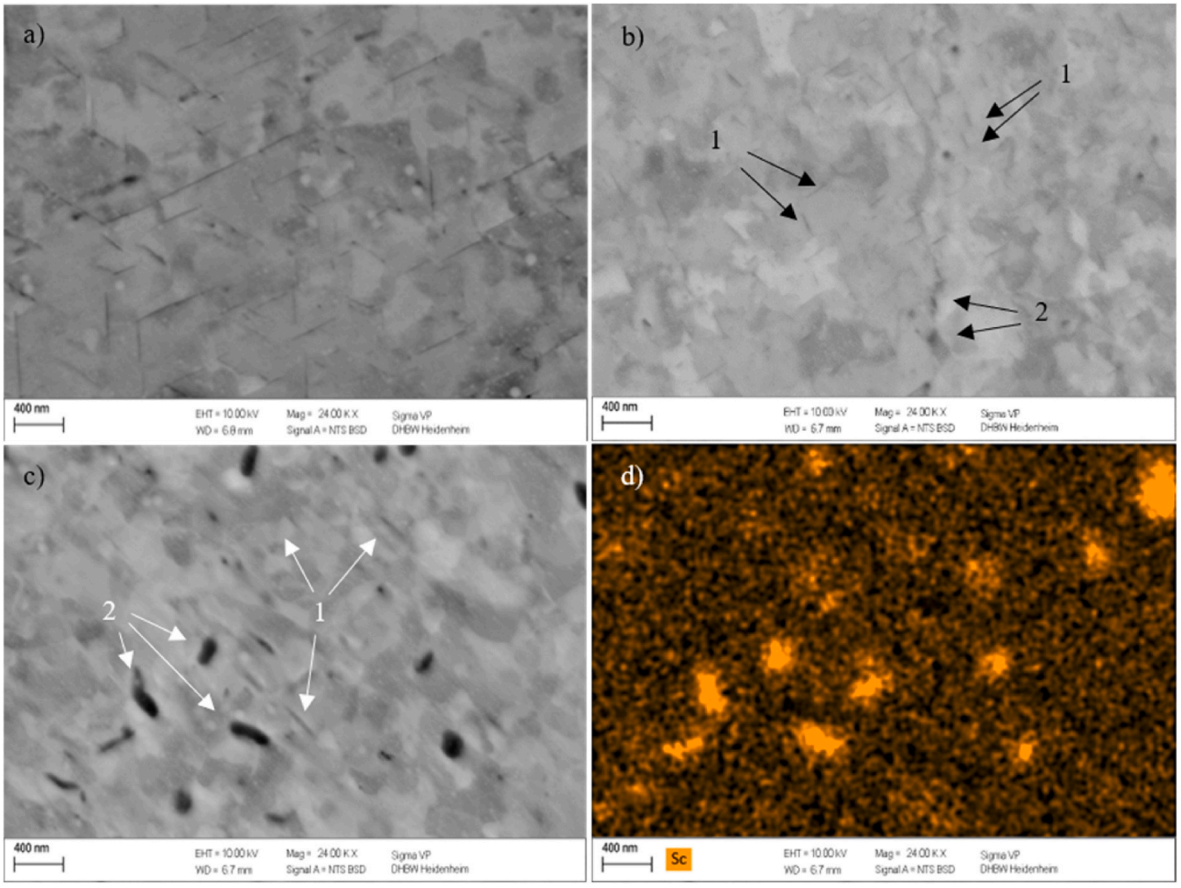

Fig. 3. SEM-BSE images of CuSc0.27 alloy aged for 48 h at 450 °C: (a) 0 %, (b) 25 %, and (c) 50 % cold-worked condition; (d) corresponding EDS Sc map of (c).

already displayed high conductivity values after short annealing time, indicating an early onset of precipitation. In contrast, the 0 % CW condition showed a delayed evolution, with a plateau in the first 6 h followed by a marked increase between 6 and 12 h. After 12 h, the increase continued more gradually, reaching 48.3 MS/m after 48 h.

3.2. X-ray diffraction analysis

X-ray diffraction (XRD) was employed to analyze the microstructural evolution of the alloys, with particular attention to matrix peaks and secondary phase formation during aging. Diffraction patterns of the solution-treated and aged CuSc0.27 alloys in the 0 % and 50 % cold-worked states, along with those of the undeformed CuSc9 master alloy, are shown in Fig. 2. Characteristic peaks of the Cu matrix were

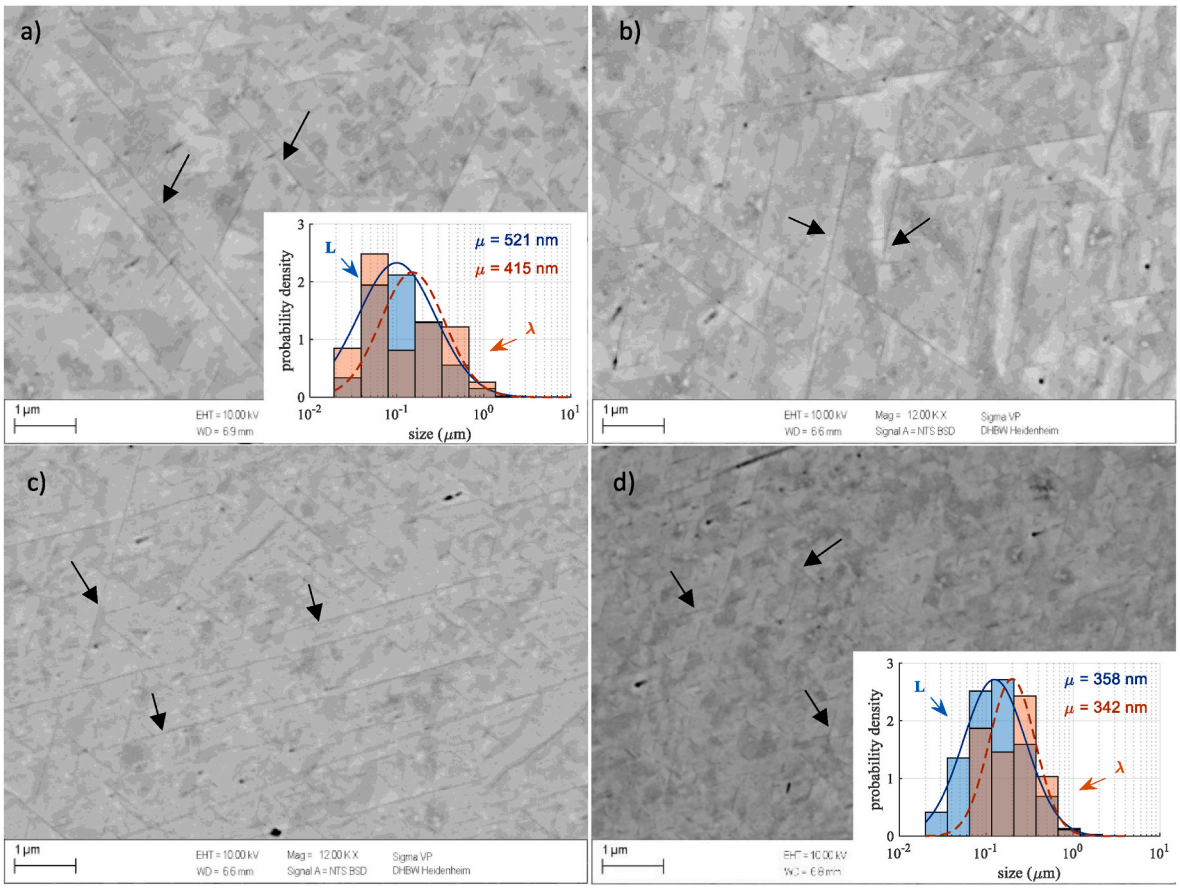

Fig. 4. SEM-BSE images of the undeformed CuSc0.27 alloy aged at 450 °C for (a) 12 h, (b) 24 h, (c) 36 h, and (d) 48 h. The size distributions of the precipitate length (L) and the interparticle spacing (λ) shown for (a) 12 h ($n_L = 999$, $n_\lambda = 60$) and (d) 48 h ($n_L = 1213$, $n_\lambda = 52$) were obtained by image analysis and statistically evaluated using log-normal fitting. n refers to the number of measured values. Mean values μ correspond to the arithmetic average. The precipitates appear as dark lines in the micrographs and are indicated by arrows.

observed in all conditions; however, the (222) Cu reflection was weak across all specimens. To identify potential Cu_4Sc reflections, a CuSc9 master alloy was investigated. Based on the equilibrium phase diagram [13,28], this composition is expected to contain only Cu and Cu_4Sc phases. Reflections distinct from those of Cu were detected at 2θ angles of approximately 30.8°, 43.15°, and 94.7°, which were attributed to the Cu_4Sc phase. The solution-treated CuSc0.27 alloy exhibited only Cu matrix peaks, indicating complete dissolution of Sc in the matrix. Upon aging, an additional peak emerged at $2\theta \approx 30.9°$ (0 % - 4 h), shifting gradually towards higher angles with prolonged aging time, indicative of precipitate formation and lattice strain relaxation. This peak is consistent with a (110) reflection of the Cu_4Sc phase, which has been reported to crystallize in a body-centered tetragonal structure with lattice parameters $a = 0.491$ nm and $c = 0.698$ nm [29]. No detectable peaks except those of the Cu matrix were observed in the 50 % cold-worked specimens (Fig. 2b). This is attributed to significant peak broadening, as evident from the comparison of the (311) peak in the undeformed and 50 % cold-worked specimens. The broadening originates from increased micro-strain and the smaller size of the precipitates, which limits their detectability via X-ray diffraction.

3.3. Microstructural analysis

3.3.1. Scanning electron microscopy

Fig. 3 presents SEM investigations utilizing the backscattered electron detector (BSE) of specimens aged 48 h at 450 °C in different cold-worked conditions. Without cold working (0 % CW, Fig. 3a), dark, plate-like Sc-enriched precipitates with lengths frequently exceeding 1 μm are observed within the Cu matrix. The observed alignment and misorientation indicate a preferred habit plane, in agreement with previous findings of Cu_4Sc precipitation along {111}Cu [15,17]. In the 25 % cold-worked condition (Fig. 3b), both semi-coherent, plate-like precipitates (1) and larger, likely incoherent, spheroidal particles (2) are observed, indicating a transition in interfacial character as the structures grow. The plate-like precipitates exhibit a pronounced crystallographic alignment, comparable to those in Fig. 3a, suggesting that they maintain a certain degree of coherency with the Cu matrix.

The 50 % cold-worked specimen (Fig. 3c) displays further coarsening, with a marked decrease in the number density of precipitates. The interparticle spacing significantly exceeds the individual precipitate size, and less preferential alignment is discernible. This morphology suggests that the particles have become largely incoherent and isotropic in growth, consistent with known Ostwald ripening [7]. The corresponding EDS elemental map (Fig. 3d) validates the Sc-rich nature of these precipitates (particles (2) in Fig. 3c).

Fig. 4 shows the microstructural evolution of the undeformed specimen aged at 450 °C for 12–48 h, based on longitudinal sections parallel to the rolling direction. With increasing aging time, the precipitates become shorter, their number density increases, and the interparticle spacing decreases. This behavior deviates from classical precipitation, which involves nucleation, growth, and coarsening accompanied by a decreasing number density [4]. At prolonged aging times, large plate-shaped precipitates were observed to fragment into smaller ones. This fragmentation, which was not observed in 50 % cold-worked samples where only small plates formed, may be related to a reduction in elastic strain energy, although the underlying mechanism remains

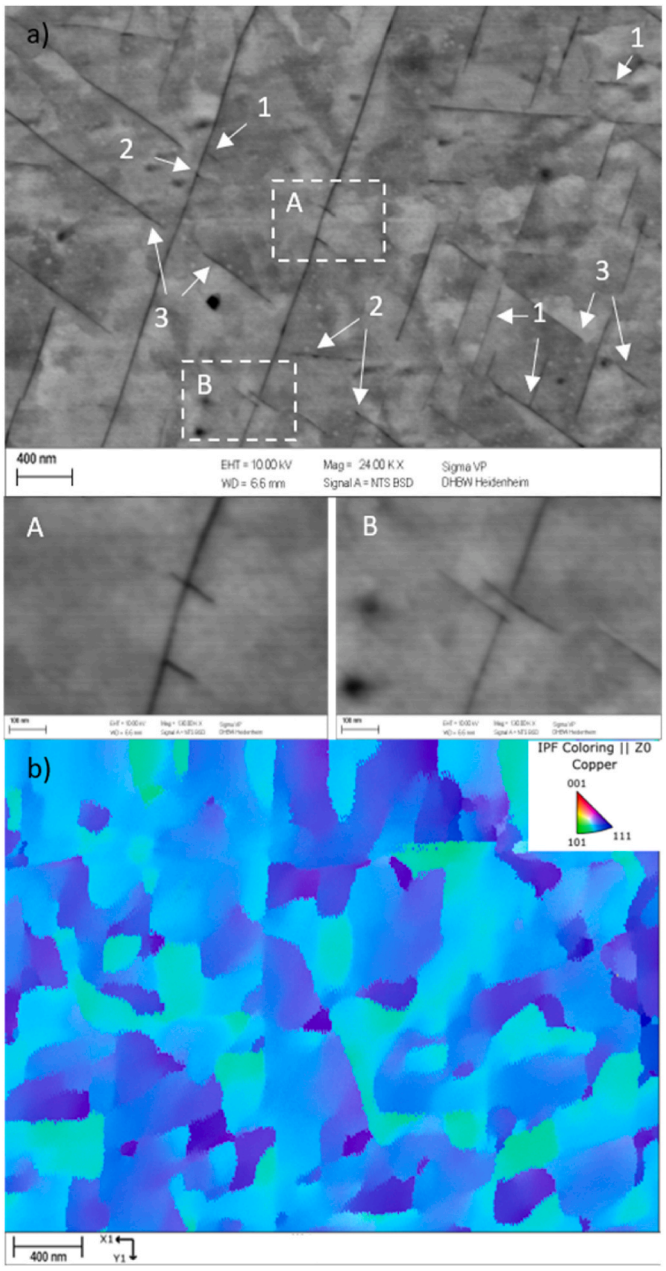

Fig. 5. (a) High-magnification SEM-BSE image of the CuSc0.27 alloy aged for 48 h at 450 °C (0 % CW) with two enlarged details (A, B). Particular features discussed in the text are marked with arrows, labelled as 1,2,3. (b) EBSD orientation map of a CuSc0.30 alloy aged at 500 °C for 48 h (0 % CW), included to provide a representative example of the crystallographic properties.

unclear.

A closer examination of the undeformed specimen aged for 48 h (Fig. 5) reveals several distinct phenomena. New precipitates frequently form adjacent to existing ones (1), suggesting a mechanism of secondary nucleation. Before their appearance, the surrounding matrix exhibits increased contrast variation (2), indicating a locally elevated scandium concentration. The new precipitates grow laterally from the sides of existing particles along specific crystallographic directions (detail A) and may detach from the original phase as growth progresses (3). Additionally, the formation of new precipitates between or at the ends of existing ones can lead to segmentation (detail B), resulting in reduced precipitate length, decreased interparticle spacing, and increased number density.

These morphological transformations are accompanied by visible changes in BSE contrast in the surrounding matrix. While the precipitates consistently appear dark grey due to their lower atomic number, local contrast variations at the precipitate–matrix interface arise from orientation-dependent backscatter efficiency. Depending on the crystallographic orientation, the matrix appears in varying shades of grey in BSE imaging [30]. This interpretation is supported by EBSD measurements (Fig. 4d), which reveal local orientation gradients in the matrix adjacent to the precipitates. These range from near-⟨111⟩ to intermediate states between ⟨111⟩ and ⟨101⟩, indicating a semi-coherent or partially coherent interface. The presence of orientation gradients and lattice distortions further supports the role of coherency strain in particle–matrix interactions, which is known to interact with dislocations and contribute to strengthening via modulus and coherency mechanisms [3].

3.3.2. *Transmission electron microscopy*

Fig. 6 presents bright-field TEM micrographs of the 0 % cold-worked Cu-Sc alloy aged at 450 °C for 6 h. An elongated, plate-like precipitate extending over several micrometers is visible in Fig. 6a. Its morphology and scale closely match those observed in SEM (cf. Fig. 4), and the presence of additional, similarly aligned precipitates suggests crystallographic alignment along a specific direction. Contrast variations around the precipitates indicate local strain fields, consistent with coherency-induced lattice mismatch between precipitates and Cu matrix. Fig. 6b shows a precipitate with multiple contrast variations along its longitudinal axis, likely caused by diffraction contrast from an additional plate-like precipitate inclined relative to the foil. This interpretation is consistent with typical contrast mechanisms in TEM.

At higher magnification, Fig. 6c reveals small, oval-shaped particles attached to an elongated precipitate. Several of these secondary precipitates exhibit a different crystallographic orientation relative to the central particle (3). Their distribution and alignment suggest nucleation and growth in close interaction with the host precipitate, possibly reflecting an early stage of lateral coarsening, consistent with the accumulations observed in the SEM image in Fig. 5a, detail A. Mismatch dislocations are visible at the precipitate–matrix interface (2), indicating local strain accommodation due to lattice misfit.

Fig. 6d shows a magnified view of the precipitate in Fig. 6b. The internal structure resolves into a moiré pattern caused by the inclined plate overlapping with the surrounding matrix. While a lamellar arrangement has been postulated previously [15], the present observations are more consistent with moiré-related contrast effects.

Fig. 7 illustrates the temporal evolution of the microstructure in the 50 % cold-worked Cu-Sc alloy aged at 450 °C for 0.25, 1, 2, and 6 h. At early aging stages (Fig. 7a), two precipitate morphologies are observed: numerous fine, homogeneously distributed clusters (1), and moiré patterns indicating plate-like precipitates (2). Quantitative analysis after 15 min reveals an average precipitate length of 9.13 nm and a width of 3.13 nm.

With increasing aging time, precipitate length significantly increases, reaching an average of 21.65 nm after 6 h. Width grows only marginally from approximately 4.5 nm at 1 h to 5.5 nm at 6 h. These results indicate that growth occurs primarily along the lateral dimension, while thickness increase is minor. Thickness mostly reflects the inclination angle to the foil. Appendix Fig. A3 presents precipitate length distributions over aging time from TEM and SEM, while the corresponding probability density functions for 0 % (Fig. A3a) and 50 % (Fig. A3b) cold-worked specimens provide the statistical basis for the reported mean values.

3.3.3. *Atom probe tomography*

To investigate precipitation processes, non-deformed specimens aged at 450 °C for 1 h and 2 h, as well as 50 % cold-worked specimens aged for 15 min, 1 h, 2 h, and 6 h, were analyzed by atom probe tomography. The cold-worked state was chosen to cover both underaged and overaged conditions.

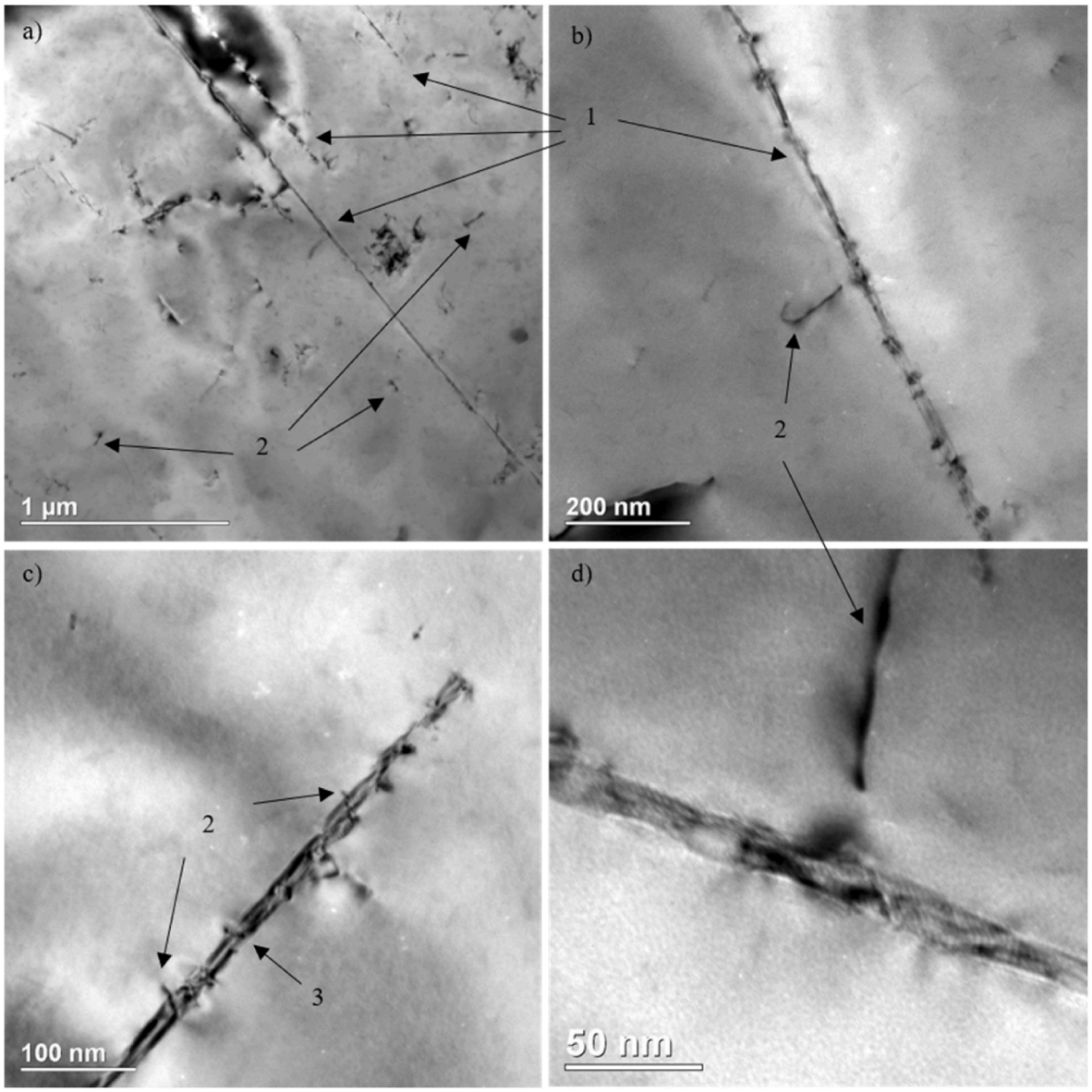

Fig. 6. Bright-field TEM images of the 0 % cold-worked Cu-Sc alloy aged at 450 °C for 6 h: (a) plate-like precipitate (1) aligned crystallographically beside dislocations (2); (b) longitudinal contrast variations along a precipitate; (c) secondary precipitates attached to a larger particle; (d) magnified view of (b), revealing moiré pattern of stacking two different or misoriented structures of matrix and precipitate. Locally varying contrast indicates mismatch dislocations at the interface.

Fig. 8a shows a reconstructed APT volume of the CuSc0.27 alloy in the 50 % cold-worked state after 1 h at 450 °C. The dataset contains about 6.7 million atoms (Cu 1+ and 2+, Sc 2+). For clarity, only 5 % of Cu atoms and all Sc atoms are shown. Despite the low global Sc concentration (1.13 at.%), two Sc-enriched precipitates are clearly resolved. To quantify the local composition, a cylindrical analysis volume consisting of 20 segments was placed perpendicular to the lamellar axis within the precipitate. The corresponding concentration profile (Fig. 8c) reveals Sc contents of up to 20 at.% within the precipitate, strongly suggesting the presence of Cu_4Sc. The spacing between the phases contains nearly pure Cu. The apparent continuous decrease of Sc at the interface arises from the inclined orientation of the lamellae relative to the analysis cylinder and the finite segment thickness. The size of the segments was chosen to ensure sufficient statistical reliability (>200 atoms per segment). The surrounding matrix contained ~0.05 at.% Sc.

A similar trend was observed in the specimen aged for 6 h (Fig. 8b), where a larger cylinder and an increased number of atoms per segment were used due to the greater size of the precipitate. The Sc-rich region extends over a broader area, reflecting the prolonged aging time and continued precipitate growth. Nevertheless, the core regions of the precipitate still reach Sc concentrations of approximately 20 at.% (Fig. 8d), while the outer regions appear enriched in Cu, leading to lower relative Sc contents near the phase boundaries.

To gain a more comprehensive understanding of the compositional distribution within the precipitate, a full three-dimensional local composition analysis was conducted. A sphere with variable radius is centered around each atom in the selected volume, such that it always includes the N-1 nearest neighbors, resulting in a total of N atoms within the sphere. The local composition in terms of the number of Sc atoms, N_{Sc}, can then be readily determined. This leads to a local composition histogram, as illustrated in Fig. 8e, with a mean Sc concentration of 19 at.%. The histogram approximately follows a Gaussian distribution. For comparison, the expected distribution for a random ideal solution is also shown, represented by a binomial distribution based on the mean concentration within the evaluated region. Notably, the experimental distribution is significantly broader than the binomial prediction. This is in stark contrast to expectations based on the Cu_4Sc line compound phase [2,13], which would theoretically yield a sharp δ-function-like peak.

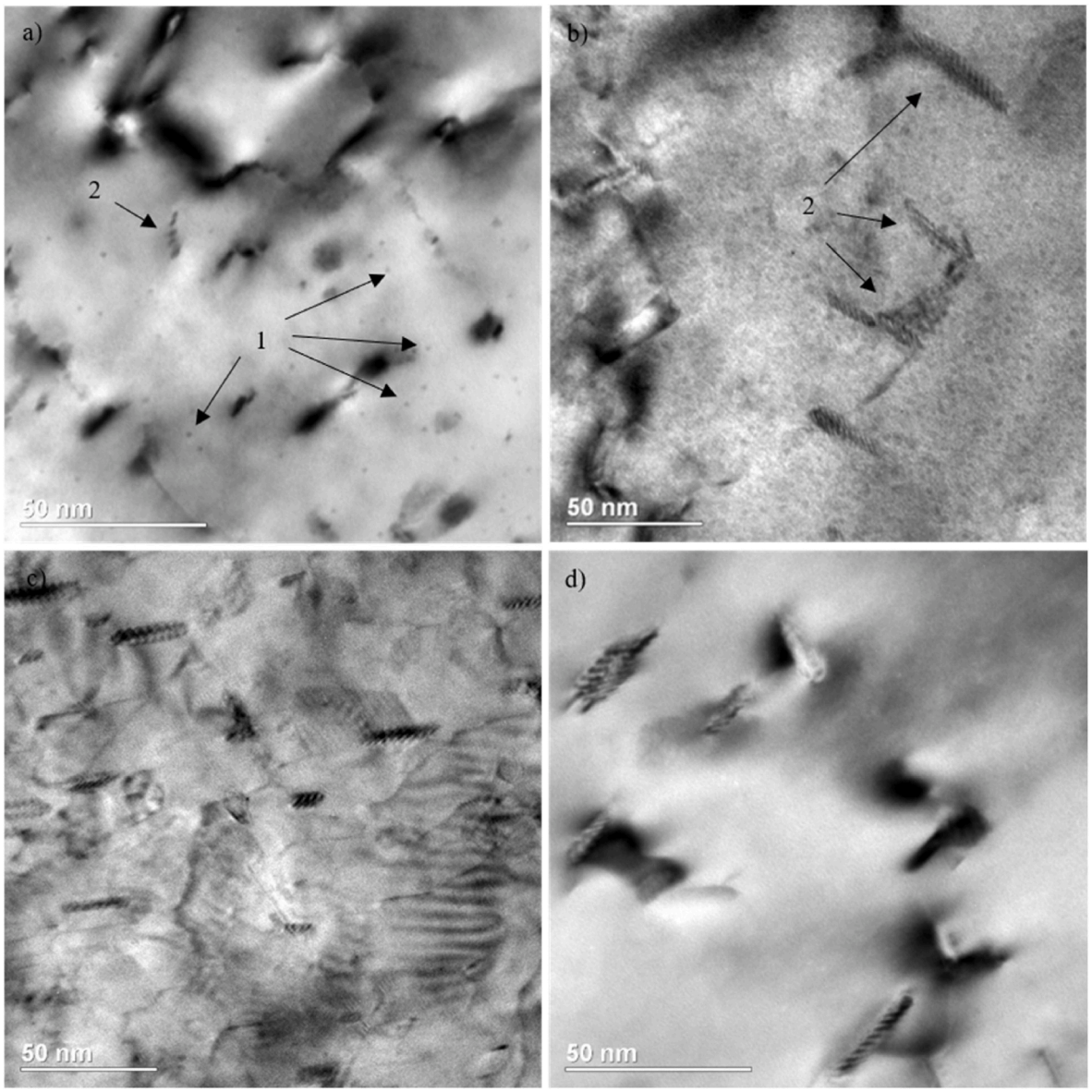

Fig. 7. Bright-field TEM images showing the microstructural evolution of the 50 % cold-worked Cu-Sc alloy aged at 450 °C for (a) 0.25 h, (b) 1 h, (c) 2 h, and (d) 6 h.

Recent studies have thoroughly investigated the broadening of such distributions [31,32], concluding that the width is strongly affected by long-ranged compositional inhomogeneities. These are attributed to limitations in APT resolution when analyzing phases of different evaporation threshold, which prevent reconstruction of a perfectly stoichiometric ordered phase and result in a natural broadening of the observed distribution. A more thorough investigation would be required to extract thermodynamic information such as mixing or demixing tendencies, as superficial analysis may lead to misleading interpretations.

To investigate scandium concentration within precipitates and its evolution during aging, cluster analyses were performed on 50 % cold-worked specimens aged 0.25, 1, 2, and 6 h at 450 °C, covering six datasets from different APT needles. Fig. 9 illustrates the local composition of individual clusters as identified by the OVITO cluster analysis algorithm. With increasing aging time, a clear growth of the clusters is observed. Importantly, the local composition calculations reveal that Sc concentrations of at least 17.5 at.% are reached in the core regions of the clusters, strongly suggesting the presence of the Cu_4Sc phase and confirming the analysis presented in Fig. 8. A gradual decrease in Sc concentration is observed toward the cluster boundaries, which likely reflects the erroneous incorporation of Cu atoms from the surrounding matrix at the phase interface.

These findings demonstrate that even after very short aging durations (0.25 h, Fig. 9a), clusters with a local composition close to the stoichiometry of Cu_4Sc can form. The cluster morphology at this early stage appears spherical, whereas with increasing aging time, particularly from 1 h onward (Fig. 9b), the precipitates morphology shifts towards a plate-like morphology.

4. Discussion

4.1. Experimental results

The evolution of strength, hardness, and electrical conductivity in Cu-Sc alloys during aging is intimately linked to the morphological and compositional development of the precipitated Cu_4Sc phases. SEM, TEM and APT confirm the formation of fine, plate-like precipitates already within the first hour of aging treatment at 450 °C, particularly in previously cold-worked specimens. In 50 % CW specimens, these

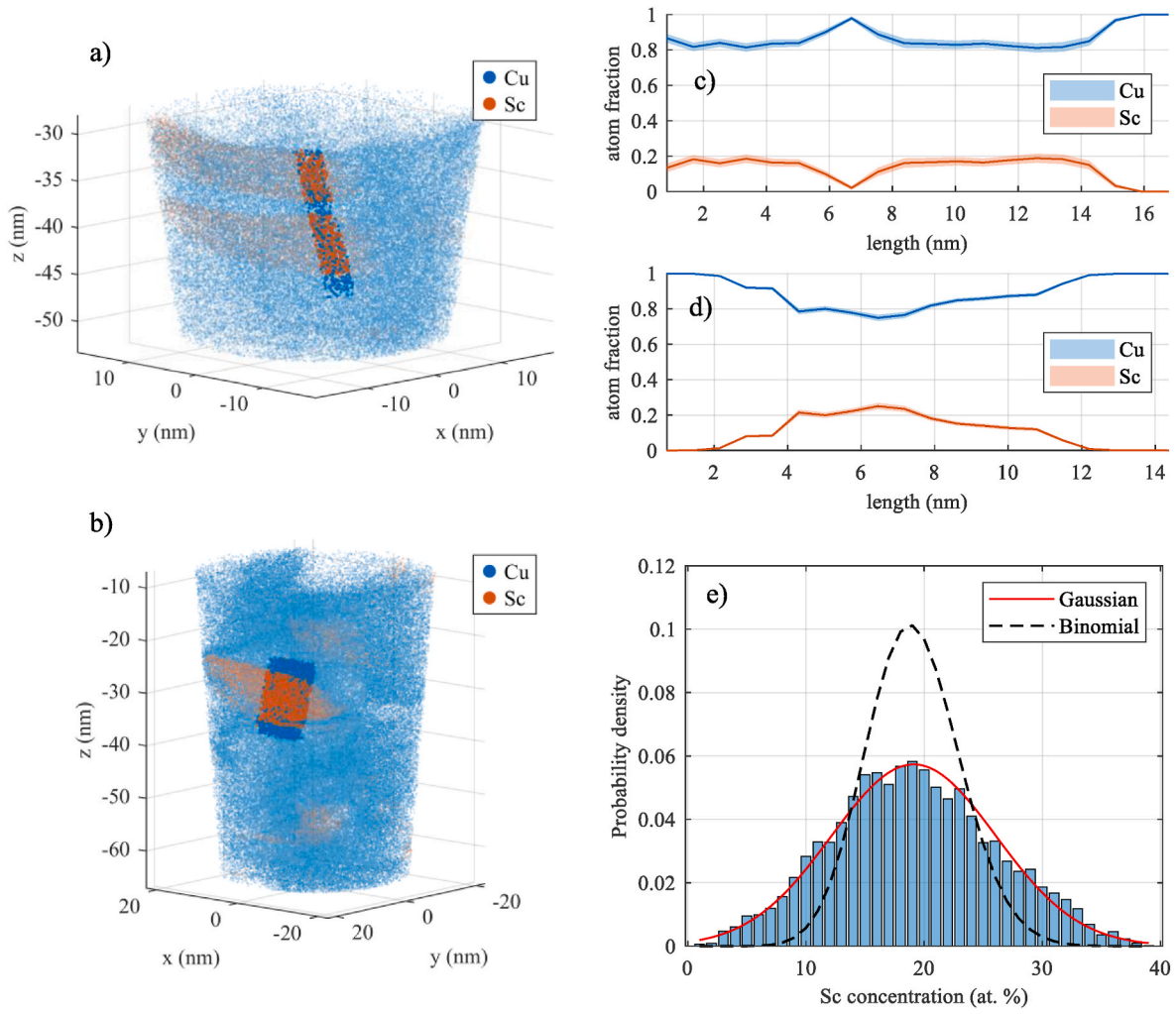

Fig. 8. APT reconstruction of the 50 % cold-worked CuSc0.27 alloy aged at 450 °C for 1 h (a) and 6 h (b), showing Sc-rich precipitates. Cu atoms are displayed at 5 % of their density. Cylindrical regions (r = 1.5 nm in (a) and r = 4.5 nm in (b)) indicate the volumes used for compositional analysis, each divided into 20 slices. Panels (c) and (d) show the corresponding concentration profiles along the cylinder axis after 1 h and 6 h of aging, respectively. Confidence bands indicate the statistical uncertainty (±σ), which was derived from the number of atoms contained in each segment. (e) Histograms of local composition using an evaluation volume of N = 100 atoms, fitted with Gaussian functions.

precipitates exhibit an average length of 20 nm, forming more densely and at earlier stages than in the undeformed state. This enhanced precipitation response is attributed to the increased dislocation density introduced by cold rolling, which promotes heterogeneous nucleation and accelerates solute diffusion along dislocations possibly additionally driven by strain fields.

Complementary insights from APT and XRD reveal the presence of coherent clusters at early aging times, consistent with a dominant coherency strengthening contribution. TEM analyses further show that even the longer, matrix-aligned phases, analyzed in SEM, exhibit pronounced strain contrast, indicating semi-coherent interfaces that contribute to strengthening. Only at advanced aging conditions larger, oval-shaped precipitates, predominantly found in cold-worked specimens (e.g., Fig. 3b and c), lose their alignment and become incoherent, thereby reducing their effectiveness as strengthening obstacles.

Correlating with these microstructural changes, the corresponding mechanical properties evolve characteristically. Hardness and tensile strength increase rapidly in cold-worked specimens, reaching a maximum after short aging times (≤1 h), followed by a gradual decline due to precipitate coarsening and static recovery. Despite softening at extended aging durations (48 h), strength and hardness remain higher to those of the non-cold-worked condition. Simultaneously, electrical conductivity increases sharply, reaching 44.9 MS/m (77 % IACS) after 1 h in the 50 % cold-rolled condition and peaking at 50.4 MS/m (87 % IACS) after 36 h. These values remain below the calculated limit (~56 MS/m), derived from the maximum Sc solubility in Cu at 450 °C (0.0065 wt%) from MatCalc [14] and the empirical Sc - conductivity relationship given in Eq. (1), indicating incomplete solute depletion and recovery due to diffusion-limited kinetics.

Regarding literature, these results underscore the decisive influence of thermal activation and deformation history on precipitation behavior. Comparable strength and conductivity values in the peak-aged condition were also reported for a Cu-0.9Hf alloy aged isothermally at 500 °C for 1 h, whereas additional thermomechanical treatment in that study led to a further increase in strength [11]. Hao et al. [15] reported a strong temperature dependence in a cryo-rolled Cu-0.4 wt% Sc alloy. Aging at 600 °C resulted in a rapid conductivity increase, accompanied by significant strength loss due to dominant recovery and recrystallization. In contrast, aging at 400 °C for 2 h led to a precipitation-induced strengthening increment of about 81 MPa between the as-rolled and peak-aged condition at a conductivity of 53 % IACS, considerably lower than the peak-aged conductivity achieved in this study. The associated microstructure in that study revealed Sc-rich precipitates with lengths of 1.5–3 nm.

In the present study, the precipitation-induced strengthening increment is significantly lower (about 20 MPa), which correlates with the

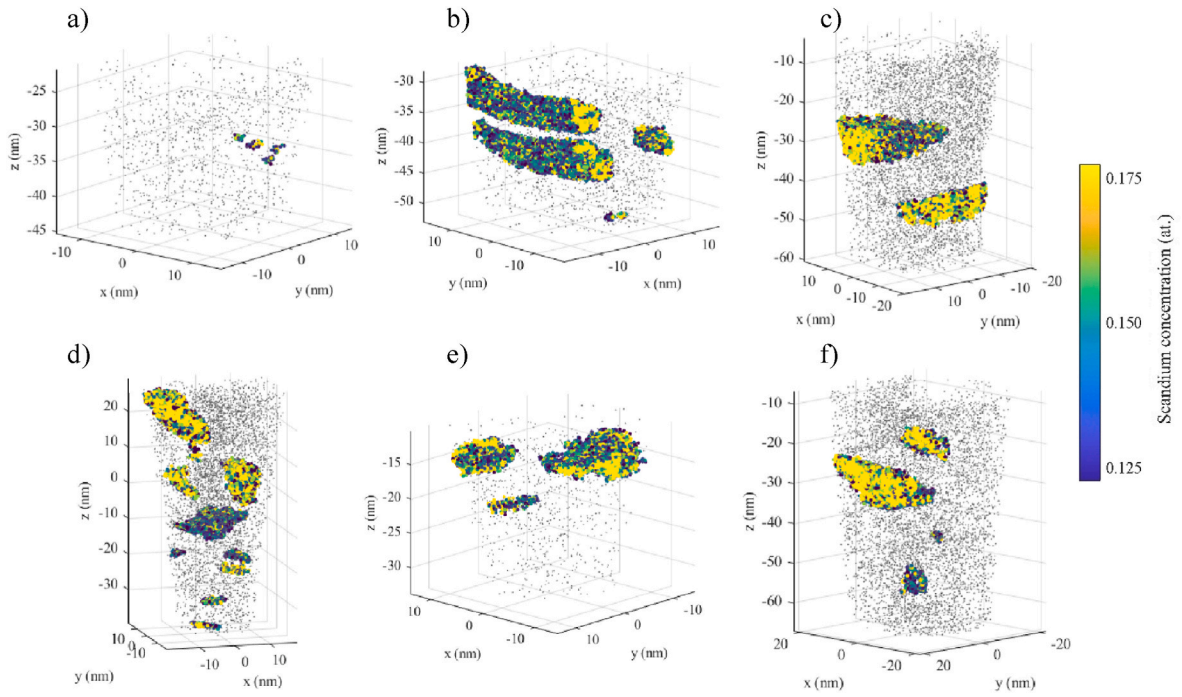

Fig. 9. Atom probe tomography data of CuSc0.27 50 % CW, aged at 450 °C for different times: (a) 15 min, (b) 1 h, (c,d) 2 h, and (e,f) 6 h. Matrix Cu atoms (displayed at 0.2 % density) are shown in grey to provide spatial context for the clusters. Clusters identified by the OVITO cluster analysis algorithm are color-coded according to their local Sc concentration. (For interpretation of the references to color in this figure legend, the reader is referred to the Web version of this article.)

presence of larger and more sparsely distributed precipitates with lengths of 9–20 nm. This difference emphasizes the critical role of deformation-induced defects in controlling precipitation kinetics. The extensive introduction of defects through cryogenic rolling likely provided a higher density of nucleation sites, promoting the formation of finer and predominantly coherent precipitates with a more pronounced strengthening effect.

Consistent with this, Dölling [17] observed a more rapid conductivity increase in undeformed Cu-0.3 wt% Sc specimens aged at 450 °C compared to the present study, underscoring the sensitivity of precipitation kinetics to solute content.

In summary, the strengthening response in Cu-Sc alloys arise from a dynamic interaction of precipitation, recovery, and solid solution hardening. The microstructural evidence and property evolution presented here establish a basis for the subsequent quantitative modeling of individual strengthening contributions under varying thermomechanical conditions as presented and discussed in the next section.

4.2. Modeling

To quantitatively capture the microstructural and mechanical evolution during aging, this section presents a modeling approach based on the experimental data obtained for both the undeformed and the 50 % cold-worked Cu-Sc alloys. Two key aspects are considered: the precipitation kinetics, inferred from electrical conductivity measurements, and the corresponding strength contributions derived from microstructural

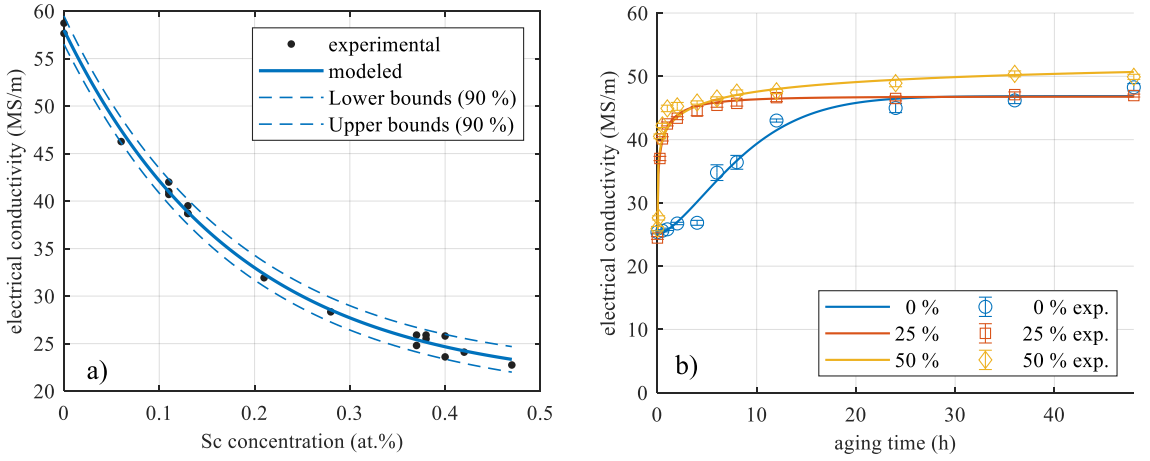

Fig. 10. Empirical modeling of electrical conductivity in Cu-Sc alloys: (a) Correlation between electrical conductivity and scandium solute concentration in the solution-annealed condition for concentrations ranging from 0 to 0.47 at% Sc (corresponding to 0.33 wt% Sc) ($R^2 = 0.99$); (b) Evolution of electrical conductivity as a function of aging time for different cold-worked states with goodness-of-fit values of $R^2 = 0.99$ (0 % CW), $R^2 = 1.00$ (25 % CW) and $R^2 = 0.88$ (50 % CW).

Table 1
Fit parameters for empirical conductivity-based precipitation kinetics model.

	0 % strain	25 % strain	50 % strain
A (MS/m)	21.87	21.80	28.42
b	0.034	1.51	0.89
n	1.50	0.42	0.25

Table 2
The micro-strain of the alloy 50 % cold-rolled after different aging durations at 450 °C.

	0.25 h	1 h	48 h
ε	0.2272 %	0.2146 %	0.1285 %

features, dislocation densities, and precipitate morphologies. The following subsections outline the methodology and parameterization used to describe these phenomena.

4.2.1. Precipitation kinetics

The evolution of electrical conductivity during aging is closely linked to the gradual depletion of Sc from the Cu-matrix as it partitions into the growing Cu_4Sc precipitates. Beyond the reduction of solute content, this increase in conductivity is also attributed to the relief of lattice distortions and internal stresses through the formation of coherent or semi-coherent precipitates [3]. To establish a quantitative relationship between the Sc-content in solid solution and the electrical conductivity, a baseline correlation was derived from data in the solution-annealed condition. This includes both previously published values [33] and experimental measurements from the current study. As shown in Fig. 10a, the conductivity decreases exponentially with increasing Sc-content in the matrix, and the relationship is captured by the empirical expression:

$$\kappa_0 = a_0 \cdot exp\left(-b_0 \cdot x_{Sc}^{ss}\right) + c_0 \tag{1}$$

where κ_0 is the electrical conductivity in MS/m, x_{Sc}^{ss} the atomic fraction of scandium in the matrix, and $a_0 = 37.97$ MS/m, $b_0 = 5.262$, and $c_0 = 19.99$ MS/m are fit parameters.

During aging, scandium precipitates from the Cu matrix, leading to a corresponding increase in electrical conductivity. Since the conductivity is inversely related to the concentration of solute atoms in the matrix, its evolution reflects the kinetics of the precipitation process, which depend on the initial cold-working condition. The following Avrami-type model was fitted to the conductivity data from both undeformed and 50 % cold-worked specimens [34]:

$$\kappa(t) = \kappa_0 + A \cdot (1 - exp(-bt^n)) \tag{2}$$

here, $\kappa(t)$ is the electrical conductivity at aging time t (in hours), κ_0 is the electrical conductivity in MS/m in solution-annealed condition, derived from Eq. (1), A is the total conductivity increase related to the amount of precipitated Sc, b describes the overall transformation rate, and n characterizes the nucleation and growth behavior. Fig. 10b shows the model fit to the measured data for different cold-working conditions. The corresponding fit parameters are given in Table 1.

4.2.2. Strengthening mechanisms

The evolution of yield strength during aging is governed by multiple concurrent strengthening mechanisms, including grain boundary strengthening ($\Delta\sigma_{gb}$), solid solution strengthening ($\Delta\sigma_{ss}$), work hardening ($\Delta\sigma_{dis}$), and precipitation strengthening ($\Delta\sigma_P$), which can occur via both the shearing ($\Delta\sigma_{cs}$) and Orowan bypass ($\Delta\sigma_{Oro}$) mechanisms. To isolate and quantify the contribution of each mechanism, established analytical models were applied and the results were compared to the experimentally determined yield strength values.

The total yield strength ($\sigma_{0.2}$) is expressed as the sum of individual strengthening contributions and a base friction stress (σ_0), which represents the intrinsic resistance to dislocation glide:

$$\sigma_{0.2} = \sigma_0 + \Delta\sigma_{gb} + \Delta\sigma_{ss} + \Delta\sigma_{dis} + \Delta\sigma_{cs} + \Delta\sigma_{Oro} \tag{3}$$

For pure copper, the friction stress σ_0 is assumed to be 25 MPa [3,35].

The individual contributions from the strengthening mechanisms are summarized in Table 4, while a comparison between the modeled and experimentally measured yield strength values is provided in Fig. 10.

4.2.2.1. Grain boundary strengthening.

To evaluate the effect of grain size on yield strength, the classical Hall-Petch relationship is employed. Based on the findings of Köster et al. [36], the Hall-Petch slope k_{HP} remains largely independent of solute content in copper-based systems. Consequently, k_{HP} is treated as constant across the investigated scandium concentrations.

Metallographic analysis revealed that the average grain size remains stable during the entire heat treatment process. Measurements conducted on both the solution-treated and overaged conditions, irrespective of prior cold deformation, show no evidence of recrystallization or grain growth, even after aging for 48 h at 450 °C. The grain size is therefore assumed to be constant with $d = 300$ µm for all calculations.

The constant grain boundary strengthening contribution $\Delta\sigma_{gb}$ is then given by Refs. [37–39]:

$$\Delta\sigma_{gb} = \frac{k_{HP}}{\sqrt{d}} \tag{4}$$

where $k_{HP} = 0.14$ MPa $m^{1/2}$ [40,41].

4.2.2.2. Solid solution strengthening.

At early stages of aging, a substantial fraction of scandium remains in solid solution, resulting in a measurable strengthening effect due to lattice distortions. As precipitation progresses, Sc-atoms are gradually depleted from the matrix and incorporated into the Cu_4Sc phase, which leads to stress relaxation in the lattice and a corresponding increase in electrical conductivity. This reduction in the solute concentration decreases the contribution from solid solution hardening.

The Sc-concentration in the matrix, c_{Sc}^{ss}, can be derived from the time-dependent electrical conductivity $\kappa(t)$ using the inverse form of the exponential model (Eq. (1)) introduced in Section 4.2.1:

$$c_{Sc}^{ss}(t) = -\frac{1}{b_0} \cdot ln\left(\frac{\kappa(t) - c_0}{a_0}\right) \tag{5}$$

here, a_0, b_0, and c_0 are empirical fitting parameters describing the electrical conductivity evolution of solution-treated and aged specimens.

The strengthening effect arising from scandium in solid solution is estimated using a power-law scaling consistent with the Labusch-type model [42,43]:

$$\Delta\sigma_{SS}(t) = k_{SS} \cdot \left(c_{Sc}^{ss}(t)\right)^{2/3} \tag{6}$$

The coefficient $k_{SS} = 767.6$ MPa was empirically determined based on tensile strength measurements of CuSc0.08 and CuSc0.27 alloys

during aging. The model thus reflects the solute strengthening contribution under the specific conditions of the present study.

4.2.2.3. Dislocation strengthening. Plastic deformation introduces a high density of dislocations into the alloy, which significantly contributes to strength. With increasing cold work, the dislocation density increases, enhancing the yield strength via dislocation interaction. After subtracting the grain boundary and solid solution contributions, the dislocation density in the cold-worked condition can be estimated from the Taylor equation [44]:

$$\Delta\sigma_{dis} = M\alpha Gb\sqrt{\rho} \tag{7}$$

where M is the Taylor factor (taken as 3.06), $\alpha = 0.2$ is a material constant typical for fcc copper alloys, $G = 46$ GPa is the shear modulus of the Cu-matrix, and $b = 0.2556$ nm is the Burgers vector. Using this relation, dislocation densities of approximately 5×10^{11} m^{-2} for the non-deformed condition and 2.5×10^{15} m^{-2} for the 50 % cold-rolled condition were calculated. These values are in good agreement with previously reported data for cold-worked copper alloys [45].

During aging, particularly in the cold-worked state, a notable decrease in dislocation density occurs, which is attributed to recovery processes at elevated temperatures. The evolution of dislocation content was quantified by XRD using the Williamson-Hall (W-H) method. The micro-strain ε was extracted from the integral breadths of selected matrix reflections and used to calculate the dislocation density via [46]:

$$\rho = \frac{16.1\ \varepsilon^2}{b^2} \tag{8}$$

where b denotes the magnitude of the Burgers vector. This approach allows a quantitative assessment of lattice distortions due to plastic deformation and their interaction with nanoscale precipitates. As listed in Table 2, the micro-strain in the 50 % cold-rolled specimens decreases with longer aging time, reflecting dislocation annihilation. The corresponding drop in dislocation density is not attributed to recrystallization, as no change in grain size was observed in the microstructure, but rather to thermally activated rearrangement and annihilation processes. Although micro-strain may also reflect coherency strains from precipitates, it is assumed in the present analysis to result exclusively from dislocations.

For the non-deformed condition, the dislocation density is assumed to remain constant throughout the aging treatment and is therefore treated as time-invariant in the model.

The calculated dislocation contribution remains significant even after prolonged aging. While earlier studies suggested that dislocation strengthening in aged Cu-Sc alloys may drop to 10–20 MPa [15], the present results indicate that even after 48 h of aging at 450 °C, the dislocation strengthening contribution in the 50 % cold-rolled sample is still approximately 144 MPa. This emphasizes the importance of dislocation structures and their interactions with the evolving precipitate morphology during recovery and overaging.

4.2.2.4. Precipitation strengthening. The mechanical strength during aging is governed by the evolving morphology, size, distribution and composition of precipitates, which influence the interaction between dislocations and obstacles. In precipitation-hardened alloys, plastic deformation arises either from dislocation shearing of coherent precipitates or from Orowan bypassing of incoherent or sufficiently large particles [3,5]. The dominant mechanism is determined by a critical precipitate radius r_c, reported by Hao et al. [15] to range between 0.51 and 0.76 nm for Cu-Sc alloys. Below this size, dislocations may shear precipitates, contributing in strengthening via coherency strain ($\Delta\sigma_{cs}$) and, to a lesser extent, due to modulus mismatch ($\Delta\sigma_{ms}$). The latter is neglected here due to the minor difference in shear modulus between the Cu matrix and the Cu_4Sc phase. Coherency strengthening relies on the elastic interaction between dislocations and the strain field induced by lattice misfit. However, since only particle sizes larger than r_c were observed in SEM and TEM analyses, coherency effects are not considered in the calculation. Accordingly, a simplified modeling approach is employed in which Orowan looping is assumed to solely govern the strengthening response.

The associated strengthening contribution is given by Ref. [47]:

$$\Delta\sigma_{Oro} = \frac{0.4MGb}{\pi\lambda}\cdot\frac{\ln(2r_{eff}/b)}{\sqrt{(1-\nu)}} \tag{9}$$

where λ is the mean interparticle spacing, determined directly from microstructural analysis based on spatial distributions of precipitates in representative SEM and TEM regions (e.g., Fig. 4a and d), and $\nu = 0.34$ is the Poisson's ratio for copper. While λ is often estimated geometrically from particle size and volume fraction [47,48] such methods are highly sensitive to the precipitate morphology. To avoid model-based uncertainties, a direct evaluation from experimental data was preferred. This approach is particularly justified as the strengthening effect in Eq. (9) is more sensitive to λ than to r_{eff}, making accurate spacing determination more critical. The effective particle radius r_{eff} was derived from TEM and SEM measurements and approximated using the relation $r_{eff} = \sqrt{L\cdot t/\pi}$, where L and t denote the average length and thickness of individual plate-like precipitates. This transformation from two-dimensional precipitation size into an equivalent spherical radius simplifies for analytical tractability and facilitates comparison across different modeling approaches, while maintaining consistency with observed projected areas.

Table 3 summarizes all relevant parameters used in the strength modeling, including results for both undeformed alloys aged for 2 h, 12 h, and 48 h and 50 % cold-rolled conditions at aging times of 2 h and 48

Table 3
Parameters used for modeling the strengthening contributions.

parameter	description	unit	0 % 2 h	0 % 12 h	0 % 48 h	50 % 2 h	50 % 48 h	Ref.
r_{eff}	Mean spherical equivalent precipitate radius	nm	16	35	31	4	16	This paper
λ	Mean interparticle spacing	nm	2517	415	342	90	184	This paper
ρ	Dislocation density	m^{-2}	5×10^{11}	5×10^{11}	5×10^{11}	6.05×10^{14}	4.07×10^{14}	This paper
c_{ss}	Residual Sc content in solid solution	at.%	0.331	0.093	0.063	0.081	0.045	This paper
α	Constant	–			0.2			[49,50]
M	Taylor factor	–			3.06			[3]
G	Shear modulus of Cu matrix	GPa			46			[1,2,7]
b	Burgers vector	nm			0.2556			[7]
k_{HP}	Hall–Petch coefficient	MPa·m$^{0.5}$			0.14			[40,41]
d	Grain diameter	µm			300			This paper

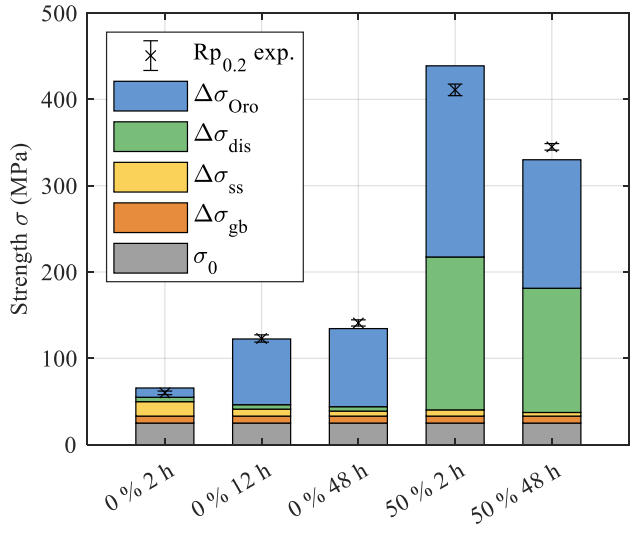

Fig. 11. Contributions of modeled strengthening mechanisms and experimental yield strength.

h.

The results of the strength modeling are compared to the experimentally determined yield strength in Fig. 11. The individual contributions from the different strengthening mechanisms are summarized in Table 4.

The calculated yield strengths are in good correlation with experimental data, showing a maximum deviation of 27 MPa (50 % CW, 2 h), corresponding to an error of 7 %. This confirms the validity of the proposed strengthening model and highlights the dominant contributions from precipitation and dislocation strengthening mechanisms.

However, some deviations are observable. Specifically, the model overestimates strength at early aging stages (0 % and 50 %, 2 h), which may indicate a significant contribution from the shearing mechanism at small particle sizes. Conversely, underestimations are found for the 48 h aged specimen (0 % and 50 % CW), which could be attributed to undetected small precipitates that fall below the detection limit of SEM. Additionally, TEM analyses cover only a limited number of particles or surface areas, potentially underrepresenting smaller precipitates and reducing the calculated Orowan strengthening contribution.

Nevertheless, the model effectively captures the key strengthening trends and thus provides valuable guidance for alloy and heat treatment design.

5. Conclusion

This study provides a detailed analysis of precipitation and deformation-induced strengthening mechanisms in Cu-0.27 wt% Sc alloys. The combined utilization of hardness, tensile test, and conductivity analysis with advanced microstructural characterization techniques (SEM, TEM, APT) enabled a detailed understanding of the aging behavior and its impact on mechanical and physical properties.

1. Peak strength was achieved after moderate cold-deformation (50 % CW) and short aging (0.5 h at 450 °C), resulting in a yield strength of 434 MPa and an ultimate tensile strength of 488 MPa at a conductivity of 42.5 MS/m (73.3 % IACS).
2. APT and TEM analyses confirmed the formation of nanoscale, platelike Cu_4Sc precipitates, with increasing Sc content at larger radii and a pronounced interaction with dislocation structures. The observed sequence of coherent clustering, coarsening, and partial loss of coherency at later stages was quantitatively linked to the precipitation kinetics and mechanical response.
3. A mechanistic strength model combining information on conductivity and particle spacing with hardening models of solid solution, dislocation, and Orowan-based precipitation reproduced the experimental trend with good agreement. Minor deviations at early stages suggest an additional contribution from a shearing mechanism for small, coherent precipitates.

The results demonstrate the considerable potential of Sc-alloying for tailoring high-strength, high-conductivity Cu materials. Future optimization may benefit from a multi-stage thermomechanical treatment strategy, in which cold deformation is used not only prior to aging but also between sequential short aging steps. This would maintain high dislocation densities and promote continuous matrix purification, potentially enabling further improvements in both strength and conductivity beyond the levels reported here.

CRediT authorship contribution statement

Ramona Henle: Writing – original draft, Visualization, Resources, Methodology, Investigation, Formal analysis, Data curation, Conceptualization. **Roham Talei:** Writing – review & editing, Investigation. **Sebastian M. Eich:** Writing – review & editing, Writing – original draft, Investigation. **Simon Kött:** Writing – review & editing, Investigation. **Julia Dölling:** Writing – review & editing, Resources. **Gerrit Nandi:** Writing – review & editing, Supervision, Conceptualization. **Andreas Zilly:** Writing – review & editing, Supervision, Resources, Conceptualization. **Ulrich Prahl:** Writing – review & editing, Supervision, Conceptualization. **Guido Schmitz:** Writing – review & editing, Supervision, Resources.

Declaration of competing interest

The authors declare that they have no known competing financial interests or personal relationships that could have appeared to influence the work reported in this paper.

Table 4
Calculated contributions of individual strengthening mechanisms.

parameter	description	unit	0 % 2 h	0 % 12 h	0 % 48 h	50 % 2 h	50 % 48 h
σ_0	Lattice friction stress	MPa			25.00		
$\Delta\sigma_{gb}$	Grain boundary strengthening	MPa			8.08		
$\Delta\sigma_{ss}$	Solid solution strengthening	MPa	16.72	8.09	5.79	7.19	4.20
$\Delta\sigma_{dis}$	Dislocation strengthening	MPa	5.09	5.09	5.09	177.14	143.91
$\Delta\sigma_{Oro}$	Precipitation (Orowan) strengthening	MPa	17.76	76.16	90.50	221.46	148.87
$\sigma_{0.2}$	Total modeled strength	MPa	65.65	122.42	134.47	438.87	330.06
$R_{p0.2}$	Experimental yield strength	MPa	60.02	123.06	141.06	411.24	345.04
	Error $\sigma_{0.2}$ - $R_{p0.2}$	%	9	0	−5	7	−4

Acknowledgments

The authors would like to thank Dr.-Ing. Oleksandr Lypchanskyi (Institute of Metal Forming, TU Bergakademie Freiberg) for his valuable support conducting the EBSD measurements. R. T. and G. S. are grateful to financial support of TEM and APT work by the Deutsche Forschungsgemeinschaft (DFG) in the frame of collaborative research center CRC1333/C03 (grant 358283783).

Appendix

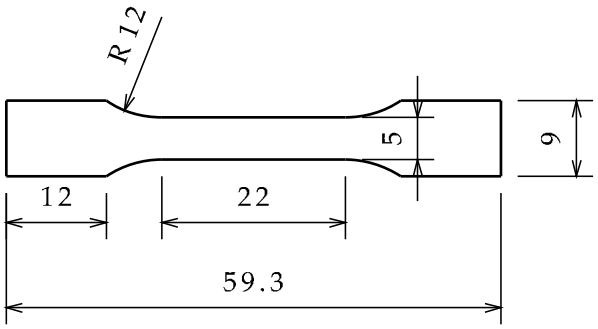

Fig. A1. Technical drawing of the tensile specimen dimensions (unit: mm) used in the study.

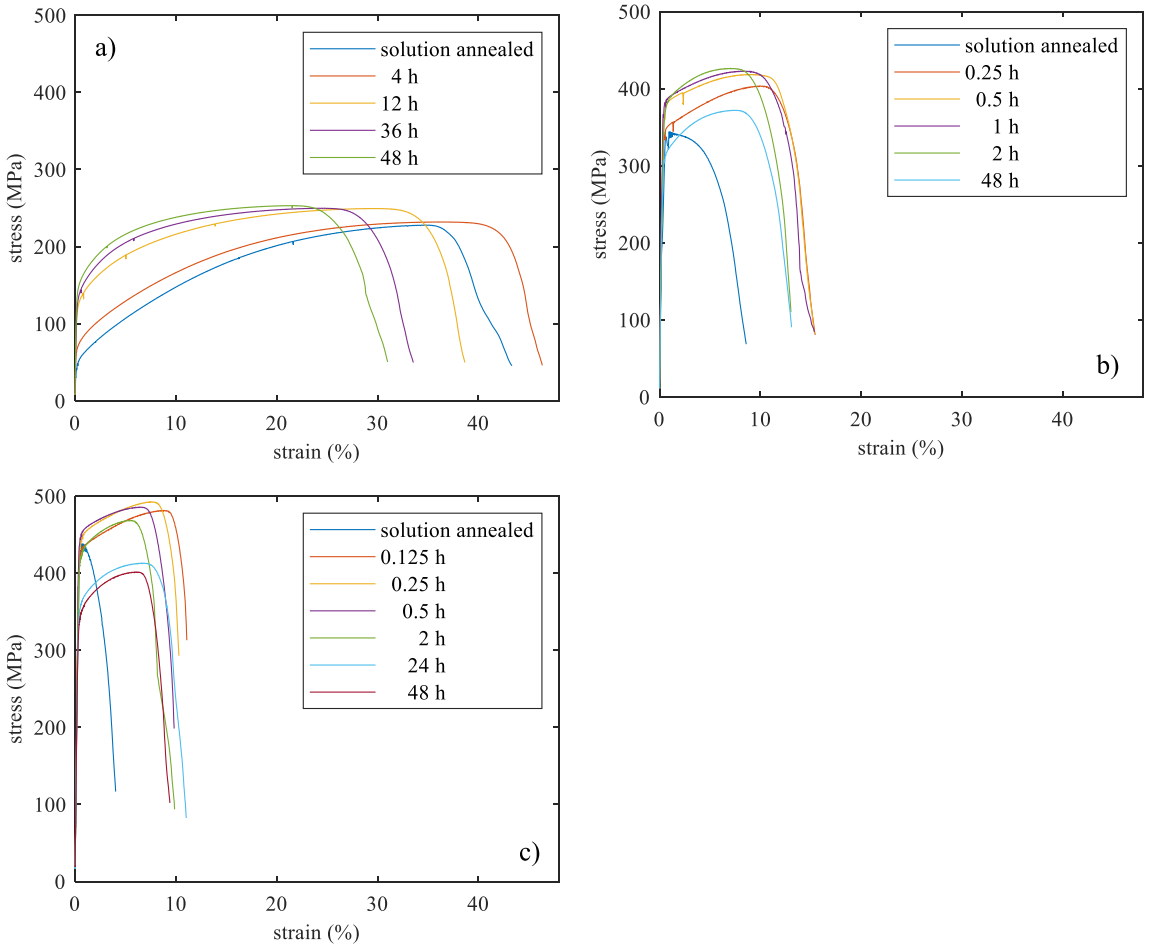

Fig. A2. Stress-strain curves of tensile tests for Cu-Sc alloys containing 0.27 wt% Sc aged at 450 °C for various times: a) 0 % CW; b) 25 % CW; c) 50 % CW.

Table A1
Measurements of relevant parameters of tensile tests Cu-Sc alloys containing 0.27 wt% Sc aged at 450 °C for various times with 0 % CW; $\overline{x}$ = arithmetic mean, s = standard deviation.

Duration of heat treatment (h)	Specimen number	E (GPa)	$R_{p0.2}$ (MPa)	R_m (MPa)	$R_m/R_{p0.2}$ (%)	A (%)	A_g (%)	μ (−)	W_B (J)
0	1	105.1	50.0	232.5	21.5	43.5	35.7	0.4	10.4
	2	119.8	52.7	224.8	23.5	40.1	33.6	0.4	9.7
	3	92.1	51.3	225.5	22.7	45.5	37.2	0.4	11.4
	$\overline{x}$	105.7	51.3	227.6	22.6	43.0	35.5	0.4	10.5
	s	11.3	1.1	3.4	0.8	2.2	1.5	0.0	0.7
4	1	122.3	69.6	232.0	30.0	46.3	36.3	0.5	12.4
	2	126.3	70.1	226.3	31.0	42.2	35.1	0.4	10.8
	3	111.4	72.2	239.7	30.1	41.3	34.1	0.4	11.2
	$\overline{x}$	120.0	70.6	232.7	30.4	43.3	35.2	0.4	11.5
	s	6.3	1.1	5.5	0.4	2.2	0.9	0.0	0.7
12	1	94.6	124.1	249.5	49.7	38.6	29.3	0.4	11.7
	2	116.6	127.6	242.6	52.6	36.7	27.5	0.4	10.8
	3	112.0	117.6	250.8	46.9	32.9	24.6	0.4	10.2
	$\overline{x}$	107.7	123.1	247.6	49.7	36.1	27.1	0.4	10.9
	s	9.5	4.2	3.6	2.3	2.4	1.9	0.0	0.6
36	1	84.2	130.0	249.6	52.1	29.7	23.0	0.4	9.1
	2	76.2	135.7	249.9	54.3	33.5	24.5	0.4	10.1
	3	115.1	133.1	249.1	53.4	27.0	20.5	0.4	8.1
	$\overline{x}$	91.8	132.9	249.6	53.3	30.1	22.7	0.4	9.1
	s	16.8	2.3	0.3	0.9	2.7	1.7	0.0	0.8
48	1	130.2	137.4	254.9	53.9	35.0	24.9	0.5	10.9
	2	124.3	145.9	253.3	57.6	31.0	21.5	0.4	9.5
	3	69.5	139.8	251.0	55.7	29.8	21.1	0.4	9.1
	$\overline{x}$	108.0	141.1	253.1	55.7	31.9	22.5	0.4	9.8
	s	27.3	3.6	1.6	1.5	2.2	1.7	0.0	0.8

Table A2
Measurements of relevant parameters of tensile tests Cu-Sc alloys containing 0.27 wt% Sc aged at 450 °C for various times with 25 % CW; $\overline{x}$ = arithmetic mean, s = standard deviation.

Duration of heat treatment (h)	Specimen number	E (GPa)	$R_{p0.2}$ (MPa)	R_m (MPa)	$R_m/R_{p0.2}$ (%)	A (%)	A_g (%)	μ (−)	W_B (J)
0	1	110.3	282.4	333.5	96.0	10.1	0.5	0.3	3.1
	2	111.2	275.4	335.0	82.2	4.9	0.9	0.3	1.6
	3	108.7	288.9	344.2	83.9	8.5	0.6	0.3	2.3
	$\overline{x}$	110.1	282.2	337.6	87.4	7.9	0.7	0.3	2.3
	s	1.0	5.5	4.7	6.1	2.2	0.2	0.0	0.6
0.25	1	117.7	328.7	398.6	82.5	12.9	9.2	0.4	4.6
	2	124.9	343.2	401.8	85.4	15.1	9.5	0.4	5.3
	3	125.3	340.3	403.5	84.3	15.4	9.6	0.4	5.4
	$\overline{x}$	122.6	337.4	401.3	84.1	14.5	9.4	0.4	5.1
	s	3.5	6.2	2.0	1.2	1.1	0.2	0.0	0.4
0.5	1	131.9	368.8	424.0	77.2	14.6	8.5	0.4	5.4
	2	113.5	360.1	418.4	86.1	15.3	8.3	0.3	5.7
	3	136.6	377.4	420.3	89.8	12.5	7.3	0.4	4.8
	$\overline{x}$	127.4	368.8	420.9	84.4	14.1	8.0	0.4	5.3
	s	10.0	7.1	2.3	5.3	1.2	0.5	0.0	0.4
1	1	134.9	372.4	421.9	88.3	14.0	8.5	0.3	5.2
	2	126.7	379.5	422.8	89.8	15.3	7.7	0.3	5.5
	3	133.2	374.7	416.0	90.1	10.8	6.6	0.4	4.2
	4	129.7	380.7	424.9	89.6	13.7	7.5	0.4	5.1
	$\overline{x}$	131.1	376.8	421.4	89.4	13.4	7.6	0.3	5.0
	s	3.2	3.4	3.3	0.7	1.6	0.7	0.0	0.5
2	1	120.9	366.1	419.6	87.2	13.1	6.7	0.3	4.7
	2	118.3	368.9	418.7	88.1	14.7	5.8	0.3	5.0
	3	96.9	370.8	426.5	86.9	12.9	6.6	0.3	4.8
	4	129.5	371.6	420.9	88.3	8.7	5.4	0.3	3.3
	$\overline{x}$	116.4	369.3	421.5	87.6	12.4	6.1	0.3	4.5
	s	12.0	2.1	3.0	0.6	2.2	0.6	0.0	0.7
48	1	120.5	318.7	382.2	83.4	15.7	8.1	0.3	5.2
	2	135.5	299.2	376.3	79.5	15.1	7.5	0.3	4.6
	3	119.6	308.0	372.0	82.8	13.0	6.9	0.3	4.2
	4	115.1	307.8	371.1	82.9	13.6	6.1	0.3	4.2
	$\overline{x}$	122.7	308.4	375.4	82.2	14.3	7.2	0.3	4.6
	s	7.7	6.9	4.4	1.5	1.1	0.7	0.0	0.4

Table A3
Measurements of relevant parameters of tensile tests Cu-Sc alloys containing 0.27 wt% Sc aged at 450 °C for various times with 50 % CW; $\overline{x}$ = arithmetic mean, s = standard deviation.

Duration of heat treatment (h)	Specimen number	E (GPa)	$R_{p0.2}$ (MPa)	R_m (MPa)	$R_m/R_{p0.2}$ (%)	A (%)	A_g (%)	μ (−)	W_B (J)
0	1	119.5	424.9	433.9	97.9	4.3	0.5	0.3	0.9
	2	119.4	423.2	438.3	98.6	3.9	0.3	0.3	0.9
	3	120.9	421.3	425.6	99.0	4.2	0.3	0.3	0.9
	$\overline{x}$	119.9	423.1	432.6	98.5	4.1	0.4	0.3	0.9
	s	0.7	1.8	5.3	0.4	0.2	0.1	0.0	0.0
0.125	1	126.6	422.3	478.1	88.3	11.1	7.3	0.4	2.9
	2	126.9	421.6	481.6	87.5	10.8	8.4	0.3	3.2
	3	124.1	417.8	480.5	74.2	11.8	8.2	0.3	3.2
	$\overline{x}$	125.9	420.6	480.1	83.4	11.3	8.0	0.3	3.1
	s	1.2	2.0	1.5	6.5	0.4	0.5	0.0	0.1
0.25	1	112.0	429.6	479.2	89.6	9.9	7.3	0.3	2.8
	2	127.8	440.7	491.7	89.6	10.4	7.9	0.3	3.1
	3	125.6	431.6	492.8	87.6	10.1	7.0	0.3	3.0
	$\overline{x}$	121.8	434.0	487.9	89.0	10.1	7.4	0.3	3.0
	s	7.0	4.8	6.1	1.0	0.2	0.4	0.0	0.1
0.5	1	120.7	441.0	481.8	91.5	8.7	6.1	0.3	2.6
	2	125.0	441.5	479.2	92.1	8.5	5.8	0.3	2.5
	3	125.5	445.1	485.6	91.7	8.3	5.9	0.3	2.5
	4	131.4	444.8	485.8	91.5	9.7	6.2	0.3	2.8
	$\overline{x}$	125.7	443.1	483.1	91.7	8.8	6.0	0.3	2.6
	s	3.8	1.9	2.8	0.2	0.5	0.2	0.0	0.1
2	1	122.3	402.5	450.9	89.3	4.8	4.5	0.3	1.3
	2	124.8	412.4	463.2	89.0	7.8	5.7	0.3	2.1
	3	122.4	418.8	468.8	89.3	4.4	4.8	0.3	1.7
	$\overline{x}$	123.1	411.2	461.0	89.2	5.7	5.0	0.3	1.7
	s	1.2	6.7	7.5	0.1	1.5	0.5	0.0	0.3
24	1	114.6	352.3	410.7	85.8	10.0	6.2	0.3	2.3
	2	116.2	353.7	413.3	85.6	11.0	6.2	0.3	2.5
	3	114.4	353.7	414.4	85.4	11.6	7.3	0.3	2.7
	4	129.9	351.3	413.8	84.9	9.4	6.4	0.3	2.2
	$\overline{x}$	118.8	352.8	413.0	85.4	10.5	6.5	0.3	2.4
	s	6.5	1.0	1.4	0.3	0.8	0.4	0.0	0.2
48	1	115.9	344.6	402.8	85.5	5.6	311.9	0.3	1.8
	2	118.0	349.9	412.2	84.9	10.7	6.4	0.3	2.4
	3	115.3	340.6	401.6	84.8	9.3	5.7	0.3	2.1
	$\overline{x}$	116.4	345.0	405.6	85.1	8.5	108.0	0.3	2.1
	s	1.1	3.8	4.7	0.3	2.1	144.2	0.0	0.3

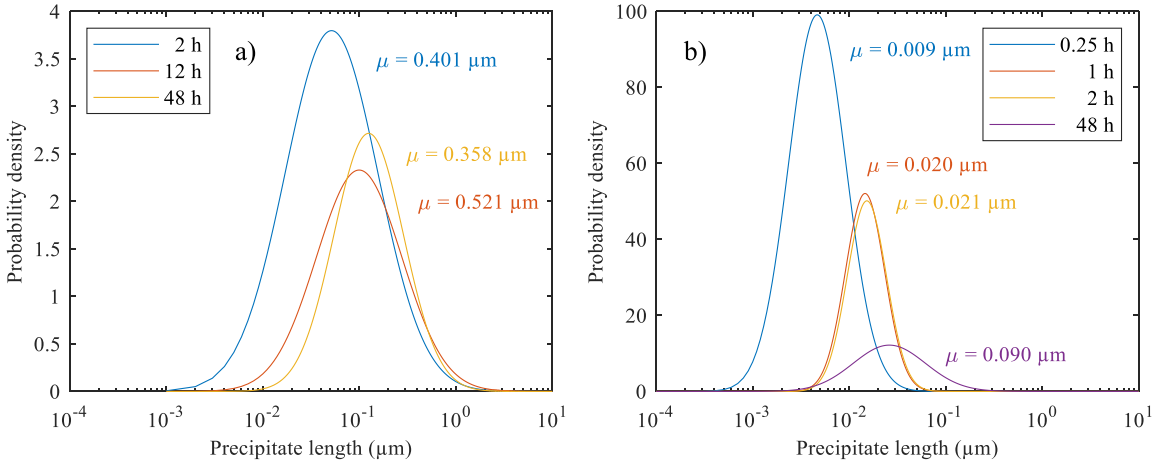

Fig. A3. Probability density function (PDF) of precipitate lengths statistically evaluated using log-normal fitting obtained from TEM and SEM measurements for various aging times at 450 °C in (a) 0 % ($n_{2h} = 24$, $n_{12h} = 999$, $n_{48h} = 1213$) and (b) 50 % ($n_{0.25h} = 62$, $n_{1h} = 104$, $n_{2h} = 61$, $n_{48h} = 307$) cold-worked Cu-Sc samples. n refers to the number of measured values. Mean values μ correspond to the arithmetic average.

Data availability

Data will be made available on request.

References

[1] J.R. Davis (Ed.), Copper and Copper Alloys, second ed., ASM International, Materials Park, OH, 2008.
[2] K. Dies, Kupfer und Kupferlegierungen in der Technik, 1967th ed., Springer, Berlin/Heidelberg, Germany, 2014.
[3] G. Gottstein, Materialwissenschaft und Werkstofftechnik: Physikalische Grundlagen, fourth ed., Springer Berlin Heidelberg, Berlin, Heidelberg, 2014.
[4] P. Haasen, Physikalische Metallkunde, 2021st ed., De Gruyter, Berlin/Boston, 2022.
[5] A.J. Ardell, Precipitation hardening, Metall. Trans. A 16 (1985) 2131–2165, https://doi.org/10.1007/BF02670416.
[6] A. Deschamps, F. Livet, Y. Bréchet, Influence of predeformation on ageing in an Al–Zn–Mg alloy—I. Microstructure evolution and mechanical properties, Acta Mater. 47 (1998) 281–292, https://doi.org/10.1016/S1359-6454(98)00293-6.
[7] T. Gladman, Precipitation hardening in metals, Mater. Sci. Technol. 15 (1999) 30–36, https://doi.org/10.1179/026708399773002782.
[8] L. Peng, H. Xie, G. Huang, G. Xu, X. Yin, X. Feng, X. Mi, Z. Yang, The phase transformation and strengthening of a Cu-0.71 wt% Cr alloy, J. Alloys Compd. 708 (2017) 1096–1102, https://doi.org/10.1016/j.jallcom.2017.03.069.
[9] K. Franczak, P. Kwaśniewski, G. Kiesiewicz, M. Zasadzińska, B. Jurkiewicz, P. Strzępek, Z. Rdzawski, Research of mechanical and electrical properties of Cu–Sc and Cu–Zr alloys, Arch. Civ. Mech. Eng. 20 (2020), https://doi.org/10.1007/s43452-020-00035-z.
[10] Y. Zhang, A.A. Volinsky, H.T. Tran, Z. Chai, P. Liu, B. Tian, Y. Liu, Aging behavior and precipitates analysis of the Cu–Cr–Zr–Ce alloy, Mater. Sci. Eng., A 650 (2016) 248–253, https://doi.org/10.1016/j.msea.2015.10.046.
[11] Y. Jiang, X. Zhang, P. Cai, P. Li, F. Cao, F. Gao, S. Liang, Precipitation behavior and microstructural evolution during thermo-mechanical processing of precipitation hardened Cu-Hf based alloys, Acta Mater. 245 (2023) 118659, https://doi.org/10.1016/j.actamat.2022.118659.
[12] J. Dölling, M. Kuglstatter, U. Prahl, H.W. Höppel, P. Ortner, B. Ott, S.F. Kracun, M. Fehlbier, A. Zilly, Analyzing the precipitation effects in low-alloyed copper alloys containing hafnium and chromium, Metals 14 (2024) 258, https://doi.org/10.3390/met14030258.
[13] H. Bo, L.B. Liu, Z.P. Jin, Thermodynamic analysis of Al–Sc, Cu–Sc and Al–Cu–Sc system, J. Alloys Compd. 490 (2010) 318–325, https://doi.org/10.1016/j.jallcom.2009.10.003.
[14] E. Povoden-Karadeniz (Ed.), MatCalc open thermodynamic database mc_cu.tdb, v0.002, 2025. http://matcalc.at.
[15] Z. Hao, G. Xie, X. Liu, Q. Tan, R. Wang, The precipitation behaviours and strengthening mechanism of a Cu-0.4 wt% Sc alloy, J. Mater. Sci. Technol. 98 (2022) 1–13, https://doi.org/10.1016/j.jmst.2020.12.081.
[16] J. Dölling, R. Henle, U. Prahl, A. Zilly, G. Nandi, Copper-based alloys with optimized hardness and high conductivity: research on precipitation hardening of low-alloyed binary CuSc alloys, Metals 12 (2022) 902, https://doi.org/10.3390/met12060902.
[17] J. Dölling, Niedriglegierte Kupferlegierungen mit Hafnium und Scandium für erhöhte mechanische Anforderungen Julia Dölling, first ed., Technische Universität Bergakademie Freiberg, Freiberg, 2024.
[18] R. Henle, J. Dölling, U. Prahl, G. Nandi, A. Zilly, DSC analysis of the effect of cold deformation on the precipitation kinetics of a binary Cu-Sc alloy, Materials (Basel, Switzerland) 16 (2023), https://doi.org/10.3390/ma16093462.
[19] E04 Committee, Test Methods for Determining Average Grain Size, ASTM International, West Conshohocken, PA, 2013.
[20] DIN EN ISO 6507-1, Metallische Werkstoffe_- Härteprüfung nach Vickers_- Teil_1: Prüfverfahren (ISO_6507-1:2018); Deutsche Fassung EN_ISO_6507-1:2018, Beuth Verlag GmbH, Berlin, 2018-07.
[21] DIN 50125, Prüfung Metallischer Werkstoffe_- Zugproben, Beuth Verlag GmbH, Berlin, 2022-08.
[22] P. Stender, C. Oberdorfer, M. Artmeier, P. Pelka, F. Spaleck, G. Schmitz, New tomographic atom probe at university of muenster, Germany, Ultramicroscopy 107 (2007) 726–733, https://doi.org/10.1016/j.ultramic.2007.02.032.
[23] M.K. Miller, Atom Probe Tomography: Analysis at the Atomic Level, Kluwer Academic/Plenum Publishers, New York, NY u.a, 2000.
[24] J. Bauch, R. Rosenkranz, Physikalische Werkstoffdiagnostik, Springer Berlin Heidelberg, Berlin, Heidelberg, 2017.
[25] M.K. Miller, R.G. Forbes, Atom-Probe Tomography, Springer US, Boston, MA, 2014.
[26] S.M. Eich, The APyT package, v0.1.1. https://test.pypi.org/project/APyT/, 2025.
[27] A. Stukowski, Visualization and analysis of atomistic simulation data with OVITO–the open visualization tool, Model. Simulat. Mater. Sci. Eng. 18 (2010) 15012, https://doi.org/10.1088/0965-0393/18/1/015012.
[28] P.R. Subramanian, D.E. Laughlin, D. J, D.J. Chakrabarti, The Cu-Sc (copper-scandium) system, Bull. Alloy Phase Diagrams (1988) 378–382.
[29] B. Kotur, V.O. Derkach, I.S. Dutsyak, A.Z. Pavlyshyn, Structure and electrical properties of ScCu4 as bulk alloy and thin film, J. Alloys Compd. 238 (1996) 81–85, https://doi.org/10.1016/0925-8388(95)02162-0.
[30] P. Kejzlar, M. Švec, E. Macajová, The usage of backscattered electrons in scanning electron microscopy, Manuf. Technol. 14 (2014) 333–336, https://doi.org/10.21062/ujep/x.2014/a/1213-2489/MT/14/3/333.
[31] J. Zheng, Extracting Thermodynamic Information from Local Composition Fluctuations in Solids Extended Theory and Its Application to Simulated and Experimental Atom Probe Data, Universität Stuttgart, 2024.
[32] J. Zheng, R. Duran, P. Diwan, G. Schmitz, S. M. Eich, Direct Measurement of the Gibbs Free Energy of Mixing via Atom Probe Tomography.
[33] R. Henle, S. Kött, N. Jost, G. Nandi, J. Dölling, A. Zilly, U. Prahl, Investigation of the solid solution hardening mechanism of low-alloyed copper–scandium alloys, Metals 14 (2024) 831, https://doi.org/10.3390/met14070831.
[34] M. Avrami, Granulation, phase change, and microstructure kinetics of phase change. III, J. Chem. Phys. 9 (1941) 177–184, https://doi.org/10.1063/1.1750872.
[35] W. Zeng, J. Xie, D. Zhou, Z. Fu, D. Zhang, E.J. Lavernia, Bulk Cu-NbC nanocomposites with high strength and high electrical conductivity, J. Alloys Compd. 745 (2018) 55–62, https://doi.org/10.1016/j.jallcom.2018.02.215.
[36] W. Köster, M.O. Speidel, Der Einfluß der Temperatur und der Korngröße auf die ausgeprägte Streckgrenze von Kupferlegierungen, Int. J. Mater. Res. 56 (1965) 585–598, https://doi.org/10.1515/ijmr-1965-560901.
[37] N.J. Petch, The cleavage strength of polycrystals, J. Iron Steel Inst. (1953) 25–28.
[38] E.O. Hall, The deformation and ageing of mild steel: III discussion of results, Proc. Phys. Soc. B 64 (1951) 747–753, https://doi.org/10.1088/0370-1301/64/9/303.
[39] W. Blum, Y.J. Li, J. Chen, X.H. Zeng, K. Lu, On the hall–petch relation between flow stress and grain size, Int. J. Mater. Res. 97 (2006) 1661–1666, https://doi.org/10.3139/146.101398.
[40] N. Hansen, Hall–petch relation and boundary strengthening, Scr. Mater. 51 (2004) 801–806, https://doi.org/10.1016/j.scriptamat.2004.06.002.
[41] Z.C. Cordero, B.E. Knight, C.A. Schuh, Six decades of the hall–petch effect – a survey of grain-size strengthening studies on pure metals, Int. Mater. Rev. 61 (2016) 495–512, https://doi.org/10.1080/09506608.2016.1191808.
[42] R. Labusch, A statistical theory of solid solution hardening, Phys. Status Solidi 41 (1970) 659–669, https://doi.org/10.1002/pssb.19700410221.
[43] P. Haasen, Verfestigung durch Mischkristallbildung, Int. J. Mater. Res. 55 (1964) 55–60, https://doi.org/10.1515/ijmr-1964-550201.
[44] The mechanism of plastic deformation of crystals. Part I.—theoretical, Proc. Roy. Soc. Lond. A 145 (1934) 362–387, https://doi.org/10.1098/rspa.1934.0106.
[45] T.G. de Sousa, V.L. Sordi, L.P. Brandão, Dislocation density and texture in copper deformed by cold rolling and ecap, Math. Res. 21 (2018), https://doi.org/10.1590/1980-5373-mr-2017-0515.
[46] G.K. Williamson, R.E. Smallman III, Dislocation densities in some annealed and cold-worked metals from measurements on the X-ray debye-scherrer spectrum, Philos. Mag. J Theor. Exp. Appl. Phys. 1 (1956) 34–46, https://doi.org/10.1080/14786435608238074.
[47] K. Ma, H. Wen, T. Hu, T.D. Topping, D. Isheim, D.N. Seidman, E.J. Lavernia, J. M. Schoenung, Mechanical behavior and strengthening mechanisms in ultrafine grain precipitation-strengthened aluminum alloy, Acta Mater. 62 (2014) 141–155, https://doi.org/10.1016/j.actamat.2013.09.042.
[48] H. Wen, T.D. Topping, D. Isheim, D.N. Seidman, E.J. Lavernia, Strengthening mechanisms in a high-strength bulk nanostructured Cu–Zn–Al alloy processed via cryomilling and spark plasma sintering, Acta Mater. 61 (2013) 2769–2782, https://doi.org/10.1016/j.actamat.2012.09.036.
[49] G. Bao, Y. Xu, L. Huang, X. Lu, L. Zhang, Y. Fang, L. Meng, J. Liu, Strengthening effect of Ag precipitates in Cu–Ag alloys: a quantitative approach, Mater. Res. Lett. 4 (2016) 37–42, https://doi.org/10.1080/21663831.2015.1091795.
[50] M. Besterci, Structure analysis of dispersion strengthening, Scripta Metall. Mater. 30 (1994) 1145–1149, https://doi.org/10.1016/0956-716X(94)90329-8.